

Flow-based network analysis of the *Caenorhabditis elegans* connectome

Karol A. Bacik,^{1,*} Michael T. Schaub,^{2,3,†} Mariano Beguerisse-Díaz,¹ Yazan N. Billeh,⁴ and Mauricio Barahona^{1,‡}

¹*Department of Mathematics, Imperial College London, London SW7 2AZ, United Kingdom*

²*naXys & Department of Mathematics, University of Namur, B-5000 Namur, Belgium*

³*ICTEAM, Université catholique de Louvain, B-1348 Louvain-la-Neuve, Belgium*

⁴*Computation and Neural Systems Program, California Institute of Technology, CA 91125 Pasadena, USA*

(Dated: September 2, 2022)

We exploit flow propagation on the directed neuronal network of the nematode *C. elegans* to reveal dynamically relevant features of its connectome. We find flow-retaining groupings of neurons at different levels of granularity, which we relate to functional and anatomical constituents of its nervous system. A systematic *in silico* evaluation of the full set of single and double neuron ablations is used to identify deletions that induce the most severe disruptions of the multi-resolution flow structure. Such ablations are linked to functionally relevant neurons, and suggest potential candidates for further *in vivo* investigation. In addition, we use the directional patterns of incoming and outgoing network flows at all scales to identify four roles for the neurons in the connectome, without pre-imposing *a priori* categories. The identified roles are then linked to functional neuronal circuits in the context of signal propagation motivated by biological input-response scenarios.

I. INTRODUCTION

The nematode *Caenorhabditis elegans* has been used as a model organism in the life sciences for half a century [1], and considerable effort has been devoted to elucidating the properties of its nervous system in relation to functional behaviour. The *C. elegans* connectome was originally charted in 1986 by White *et al* [2] and has been further refined by analysis and experiments [3], most recently in the work of Varshney *et al* [4]. Using experimental techniques such as laser ablations, calcium imaging, optogenetics and sonogenetics, researchers have examined functional properties of individual neurons in connection with motion, learning, or information processing and integration [5–9]. Other studies have quantified the characteristics of the motion of *C. elegans*, and how these change upon genetic mutations [10–12].

With the increased availability of data from such experiments, there is a need to integrate current knowledge about individual neurons into a comprehensive picture of how the network of neurons operates [2, 4, 13]. A number of studies have reported network characteristics of the *C. elegans* connectome: it is a small-world network [14] satisfying mathematical criteria of efficiency [15], with a heavy-tailed degree distribution [16] and a core-set of highly-connected, ‘rich club’ neurons [17]. Furthermore, the analysis of modules in the network has shown that certain strongly coupled clusters of neurons can be linked to biological functions [18–22]. Such observations suggest that a system-wide analysis of the connectome can provide valuable functional information. However, finding simplified mesoscale descriptions that coherently aggregate how information propagates in the directed connectome across multiple scales remains a challenge [23].

In this work, rather than focusing on structural features of the network, we analyse the directed and weighted *C. elegans* connectome from a flow-based perspective. Our methods use diffusive processes on graphs as a simple means to link features of the directed network and propagation dynamics. While diffusive flow is a simplification of the actual propagation in the nervous system of *C. elegans*, we can still gain insight into network properties of dynamical interest [4]. We exploit these ideas in two ways. Firstly, we investigate flow-based partitions of the connectome across multiple scales using the Markov Stability (MS) framework for community detection [24–26]. Our analysis detects subgroups of neurons that retain diffusive flows over particular time scales [27] taking into account edge directionality [26, 28]. We then mimic neuronal ablations computationally, and check *all* possible single and double ablations in the connectome to detect the most disruptive of the flow organisation. Secondly, we extract alternative information of the directed network flows through the Role Based Similarity (RBS) framework [29–31]. Without pre-imposing categories *a priori*, RBS classifies neurons into flow roles, directly extracted from the asymmetric patterns of incoming and outgoing network flows at all scales. We then mimic ‘stimulus-response’ experiments [5, 7, 32] in which signals propagate through the network starting from well-defined sets of input neurons linked to particular biological stimuli. The time courses of neuronal flows reveal features of information processing in *C. elegans*, in relation to the obtained flow roles. Our computational analyses are consistent with experimental findings, suggesting that our framework can provide guidance towards the identification of potential neuronal targets for further *in vivo* experiments.

* karol.bacik13@imperial.ac.uk

† michael.schaub@unamur.be

‡ m.barahona@imperial.ac.uk

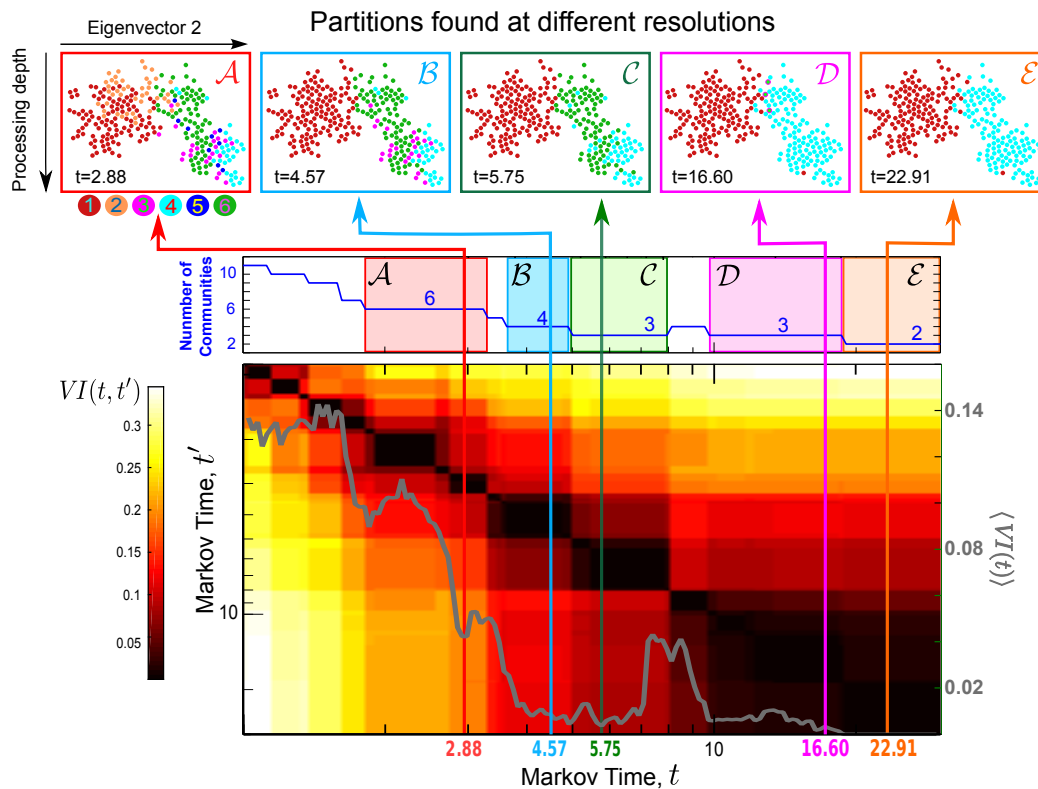


Figure 1. **Flow-based multiscale partitioning of the connectome of *C. elegans*.** Using Markov Stability, we detect flow-based partitions in this directed network at all scales. Here we show the medium to coarse Partitions \mathcal{A} to \mathcal{E} (top panel), found as optimal at the indicated Markov time intervals (see Fig. S1 in *SI* for the full sweep of Markov times). Partitions \mathcal{A} - \mathcal{E} are persistent, as signalled by extended time plateaux in $VI(t, t')$, and robust with respect to the optimisation, as signalled by dips in the variation of information $\langle VI(t) \rangle$ (see Methods).

II. RESULTS

Our analysis uses the *C. elegans* data published in Ref. [4] (see www.wormatlas.org/neuronalwiring.html). To represent the *C. elegans* connectome, we use the two-dimensional network layout given by [4], i.e., neurons are placed on the plane according to their normalised Laplacian eigenvector (x -axis) and processing depth (y -axis), as seen in Fig. 1 (top panel). We study the largest weakly-connected component of this network, which contains 279 neurons with 6394 chemical synapses (directed) and 887 gap junctions (bidirectional). Reference [4] also provides the position of the soma of each neuron along the body of the worm, and classifies each neuron as either sensory (S), interneuron (I) or motor (M).

A. Flow-based partitioning reveals multi-scale organisation of the connectome

To reveal the multi-scale flow organisation of the *C. elegans* connectome, we use the Markov Stability (MS) framework described in Sec. IV C. Conceptually, MS can be understood as follows. Imagine that a drop of ink (signal) is placed on a node and begins to diffuse along

the edges of the graph. If the graph lacks structural organisation (e.g., random), the ink diffuses isotropically and rapidly reaches its stationary distribution. However, the graph might contain subgraphs in which the flow is trapped for longer than expected, before diffusing out towards stationarity. These groups of nodes constitute dynamical, flow-retaining communities in the graph, usually signifying a strong dynamic coupling within and a weaker coupling to the rest of the network. If we allow the ink to diffuse just for a short time, then only small communities are detected, for the diffusion cannot explore the whole extent of the network. If we observe the process for a longer time, the ink reaches larger parts of the network, and the flow communities thus get larger. By employing dynamics, and in particular by scanning across time, MS can thus detect cohesive node groupings at different levels of granularity [26, 27, 33]. In this sense, the time of the diffusion process, denoted *Markov time* in the following, acts as a resolution parameter.

The flow-based community structure of the *C. elegans* connectome at medium to coarse levels of resolution is shown in Fig. 1. The full scan across all Markov times is shown in Fig. S1 in the Supplementary Information (*SI*) and the Supplementary Data. As described above, the partitions become coarser as the Markov time t increases,

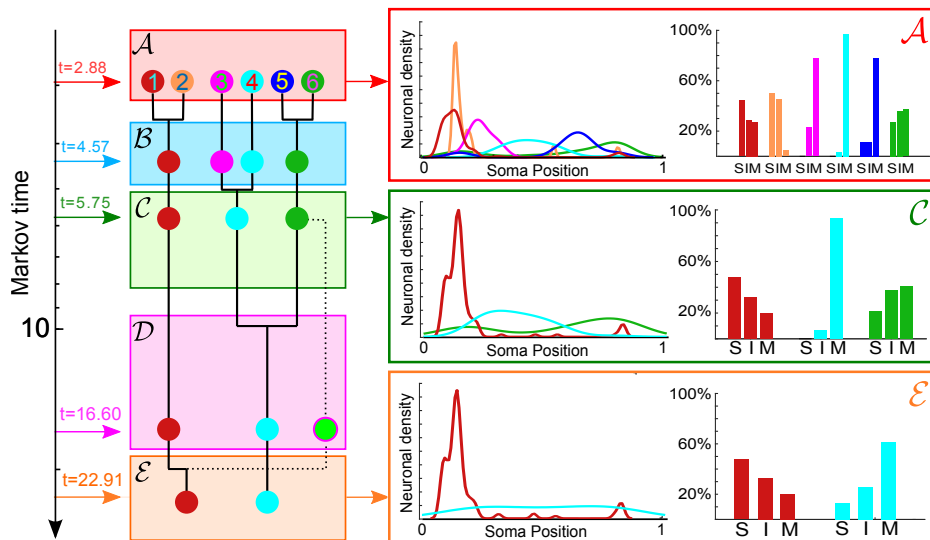


Figure 2. **Community structure and biological features.** Left: As indicated by the dendrogram, the partitions obtained have a quasi-hierarchical organisation. Middle: The smoothed spatial densities of neurons in each community for the different partitions show how the communities are spatially grouped according to soma positions. The merging of groups over Markov time largely retains this spatial structure. Right: Percentages of sensory (S), inter- (I) and motor (M) neurons in each community showing functional segregation in the groupings.

from the finest possible partition, in which each node forms its own community, to the dominant bi-partition at long Markov times. The sequence of partitions exhibits an *almost hierarchical* structure, with a strong spatial localisation linked to functional and organisational circuits (see Fig. 2 and Fig. S2 of the *SI*). These findings are in agreement with the spatial localisation of functional communities often found in brain networks [23], as well as the hierarchical modularity exhibited by the *C. elegans* connectome as reported in Ref. [34]. Remarkably, our community detection method does not enforce a hierarchical agglomeration of communities; hence the observed quasi-hierarchy and spatial localisation is an intrinsic feature of the *C. elegans* connectome.

At long Markov times, we find robust partitions containing 6 to 2 communities, denoted \mathcal{A} to \mathcal{E} in Fig. 1. Partition \mathcal{A} comprises six communities of varying sizes (from 9 to 104 neurons), well localised along the body of the worm, as seen in Fig. 2 (c.f. Section 2.2 in www.wormatlas.org/neuronalwiring.html). The two large communities (C1 and C2) have head ganglia neurons of all three functional types (S, I, M). In particular, C1 contains ring motor neurons and interneurons as well as the posterior neurons ALN and PLN, whereas C2 specifically gathers amphid neurons (e.g., AWAL/R, ASKL/R, ASIL/R, AIYL/R) which feature prominently in the navigation circuit responsible for exploratory behaviour [35]. Communities C3, C4 and C5 in Partition \mathcal{A} consist predominantly of ventral cord motor neurons, differentiated by their soma position along the body (Fig. 2): C3 contains frontal motor neurons (e.g. VD1 to VD3); C4 consists of mid-body motor neurons (e.g.

VD4 to VD8); C5 comprises posterior motor neurons (e.g. VD9 and VD10). Such partitioning is consistent with the motor neuron segmentation model proposed for *C. elegans* in Ref. [36]. Finally, C6 contains highly central neurons such as AVAL/R or PVCL/R, which have been found to belong to a *rich-club* [17], as well as interneurons linked to mechanosensation and tap withdrawal functional circuits [20].

The coarser Partitions \mathcal{B} and \mathcal{C} are quasi-hierarchical merges of \mathcal{A} (Figs. 1 and 2). For instance, Partition \mathcal{C} has three groupings: head ganglia (merged C1 and C2), frontal motor neurons (merged C3 and C4), and a tail subgroup (merged C5 and C6). Interestingly, at later Markov times, we obtain the distinct, coarser 3-community Partition \mathcal{D} , which exemplifies how our method does not enforce a strict hierarchy in the multi-scale structure. The three groups in Partition \mathcal{D} include a notable community of only three nodes (interneurons AVFL/R and AVHR), which appear as a cohesive group only at this particular timescale. Prominent functional roles of AVF and AVH neurons have been noted previously [4, 37]: both AVF neurons are responsible for coordination of egg-laying and locomotion [38]. In addition, spectral analyses of the gap-junction Laplacian have shown that AVF, AVH, PHB and C-type motor neurons are strongly coupled [4]. Finally, the two communities in the coarsest Partition \mathcal{E} split the connectome anatomically into a group with head and tail ganglia (red), and another group predominantly with motor neurons (cyan).

B. The effect of single and double neuron ablations on flow-based communities

Laser ablation experiments are invaluable to probe the functional role of neurons [5–7], but are time consuming and technically challenging. We have used our computational framework to assess the effect that an ablation of a single neuron, or of a pair of neurons, has on the signal flow in the connectome. To this end, we compare the flow-based partitions obtained for the ablated connectome against the original network. If an ablation creates large distortions in the flow structure, the partitions of the ablated network will change drastically or become less robust compared to those found in the unablated network. We have carried out a systematic computational analysis of *all* single and double neuron ablations in the connectome.

1. Single ablations: disrupting the robustness and make-up of partitions

a. Ablations that alter the robustness of partitions: To find ablations that have a strong effect on the robustness of Partitions \mathcal{A} – \mathcal{E} , we detect node deletions that induce sustained changes in the robustness $\langle VI(t) \rangle$, i.e., they appear as outliers with respect to a Gaussian Process fitted to the $\langle VI(t) \rangle$ of the ensemble of *all* single node ablations (Fig. 3). For details, see Section IV D.

Only seven single ablations satisfy our criterion for a major disruption of any of the Partitions \mathcal{A} – \mathcal{E} (Fig. 3b) The ablations of interneuron PVCR or of the motor neuron DD3 both decrease the robustness of Partition \mathcal{A} . Interestingly, PVCR (C6) and DD3 (C4) receive many incoming connections from their own community. Furthermore, both of these neurons are critical for motor action: PVCR drives motion whereas DD3 coordinates it. Another important ablation is that of interneuron AVKL, which links community C1 (head) with community C3 (ventral cord) and community C6 (rich club). The increased robustness of the community structure upon ablation of AVKL would indicate a decreased communication between these groups. The function of AVKL is uncharted at present [39], so any behavioural changes would need experimental investigation.

For Partition \mathcal{B} , there are three important ablations. The ablations of DD3 (again) or of VD2 (another D-type motor neuron yet on the ventral side) are both disruptive, as is the ablation of AIBL, an amphid interneuron. AIBL acts as a bridge between communities C1 and C2, which merge in Partition \mathcal{B} (Fig. 2). The prominent role of other amphid interneurons will become apparent in the double ablations studied in the next section.

Partition \mathcal{C} is rendered non robust by the ablations of VB8 (a motor neuron responsible for forward locomotion) or of interneuron DVC, with are both in community C5. DVC has links with communities C3, C4, C5 and C6; hence its ablation affects the subsequent merging of these

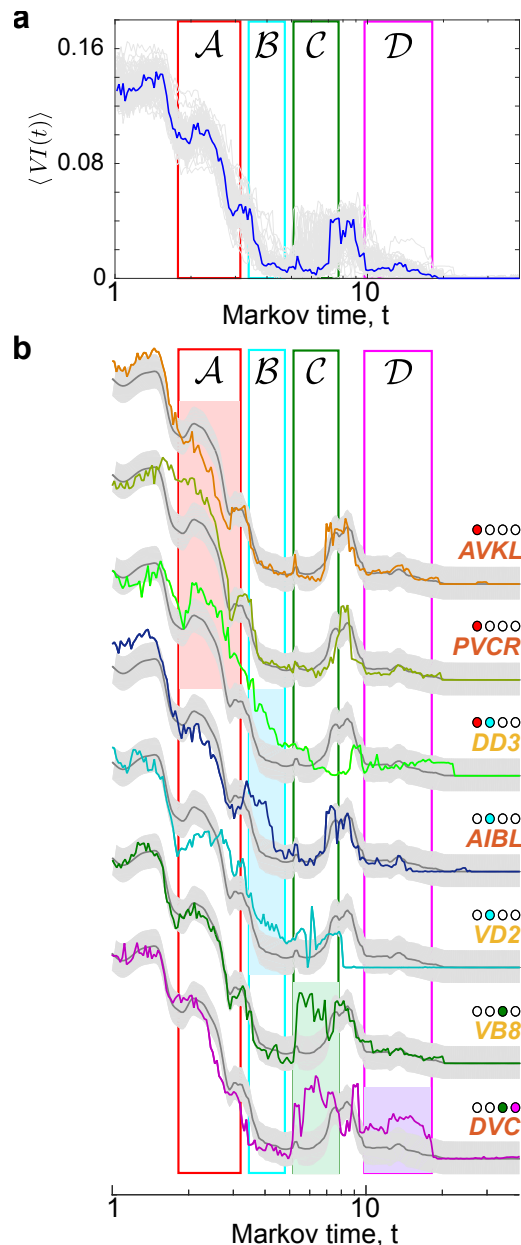


Figure 3. **Single ablations that alter the robustness of partitions.** (a) Ensemble of $\langle VI(t) \rangle$ profiles of *all* single node ablations (light gray lines) and the unablated connectome (blue). A Gaussian process (GP) is fitted to the ensemble of single ablations. (b) The GP is described by the mean $\mu(t)$ (dark grey line) and standard deviation (grey bands). Sustained outliers from the GP are identified using a statistical criterion to find seven ablations that affect the different partitions, as indicated by the coloured dots (see Methods).

groups. Note that the ablation of DVC reduces the robustness of both 3-way Partitions \mathcal{C} and \mathcal{D} , thus blurring the spatial organisation of motor neurons. This indicates that DVC might integrate feedback from different parts of the body, in accordance with the fact that it has the highest number of gap junctions in the connectome, as

well as substantial chemical synapses [40].

b. Ablations that alter the make-up of the optimal partitions: To measure how much the make-up of a partition is affected by an ablation, we use the community variation CV , defined in Eq. (13). A high value of $CV_{[i]}(\mathcal{P})$ indicates a large disruption in partition \mathcal{P} under the ablation of neuron i . Figure 4 shows the single ablations with high CV with respect to Partitions \mathcal{A} - \mathcal{E} , as detected through a statistical criterion based on inter-percentile ranges (see Section IV D). Interestingly, none is a sensory neuron, indicating that the ablation of sensory neurons is not influential for global flow at medium to coarse scales, although they can have strong local effect on the propagation of a particular stimulus.

Certain ablations are completely destructive of Partitions \mathcal{A} and \mathcal{B} . In particular, the ablations of DD3 or SMDDR induce severe changes in the network flow, so that no partition similar to \mathcal{A} is found at any Markov time. In general, ablations of D-type motor neurons coordinating motion (e.g. DD2, DD3, VD1, VD2) have particularly severe effects for the medium resolution Partitions \mathcal{A} and \mathcal{B} . Interestingly, D-type motor neurons have significantly higher PageRank (median 0.0092 compared to median of 0.0018 in the network; $p = 1.7 \times 10^{-7}$; one-sided exact test), and their synapses are critically embedded edges with few alternative routes [37]. Note that, although robustness and make-up of partitions reflect different effects, the ablation of motor neurons DD3 and VD2 substantially alters both (see Figs. 3 and 4a). In addition, the ablation of any of the command neurons AVAR/L has important effects on Partition \mathcal{C} . AVAR/L are highly central neurons (with the highest in- and out-degree in the connectome) and our method confirms that their ablation introduces heavy distortions in the global flow of the connectome. Finally, we observe that the coarsest partitions \mathcal{D} and \mathcal{E} are strongly perturbed upon ablation of ring motor neuron RMDVL. Experiments have shown that ablating any of the RMD neurons diminishes the head-withdrawal reflex [1].

Further confirmation of the importance of inter- and motor neurons is given in Figure 4b, where we show the CV of single ablations averaged over the three types (S, I, M). On average, motor neurons have a larger effect on local organisation, as reflected by the high CV for the finer Partitions \mathcal{A} and \mathcal{B} , whereas interneurons induce larger changes in global flows, as shown by larger CV for the coarser Partitions \mathcal{D} and \mathcal{E} .

2. Double ablations: beyond additive effects

We have also performed an exhaustive *in silico* exploration of all possible 38781 two-neuron ablations. Specifically, we look for synergistic pairs of neurons, i.e. pairs whose simultaneous ablation induces supra-additive disruption. To this end, we compare the CV for each double ablation to the averaged CV of the corresponding two single ablations, and use Quantile Regression to identify

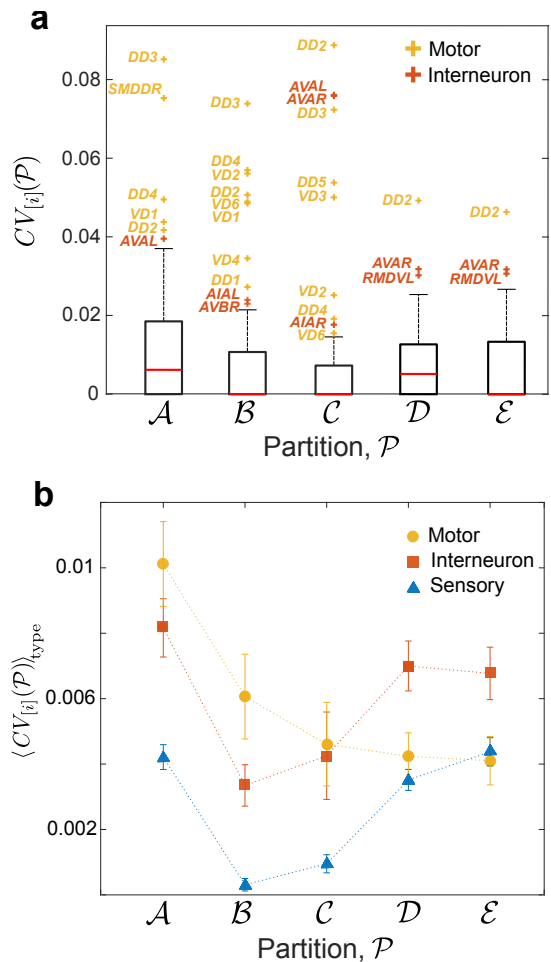


Figure 4. **Effect of single ablations on the make-up of different partitions as measured by the community variation.** (a) The disruption of every single mutation with respect to Partitions \mathcal{A} - \mathcal{E} is quantified through $CV_{[i]}(\mathcal{P})$, as defined in Eq. (13). The distribution of $CV_{[i]}$ is represented by its median (red line) and the inter-percentile range (IPR) between the 10th and 90th percentiles (box). The whiskers correspond to the IPR for each partition, and the single ablations detected as outliers are labelled. (b) Effect of the single ablations $CV_{[i]}(\mathcal{P})$ for each partition averaged over each type: sensory (blue), inter- (red) and motor neurons (yellow). On average, single ablations of motor neurons induce larger changes on the finer Partitions \mathcal{A} and \mathcal{B} , whereas ablations of interneurons have a larger effect on the coarser Partitions \mathcal{D} and \mathcal{E} . The error bars are the standard error of the mean.

double ablations with a combined effect significantly beyond the merely additive (see Section IV D 2).

We focus on disruptions to Partitions \mathcal{A} and \mathcal{D} , as prototypical of the medium and coarse resolutions, respectively (Figure 5). We select the top 1% of ablations for each partition according to their supra-additive effect. Interestingly, 85% of the top supra-additive double ablations for Partition \mathcal{A} contain at least one interneuron, whereas 90% of the top supra-additive double ablations for Partition \mathcal{D} contain at least one motor neuron

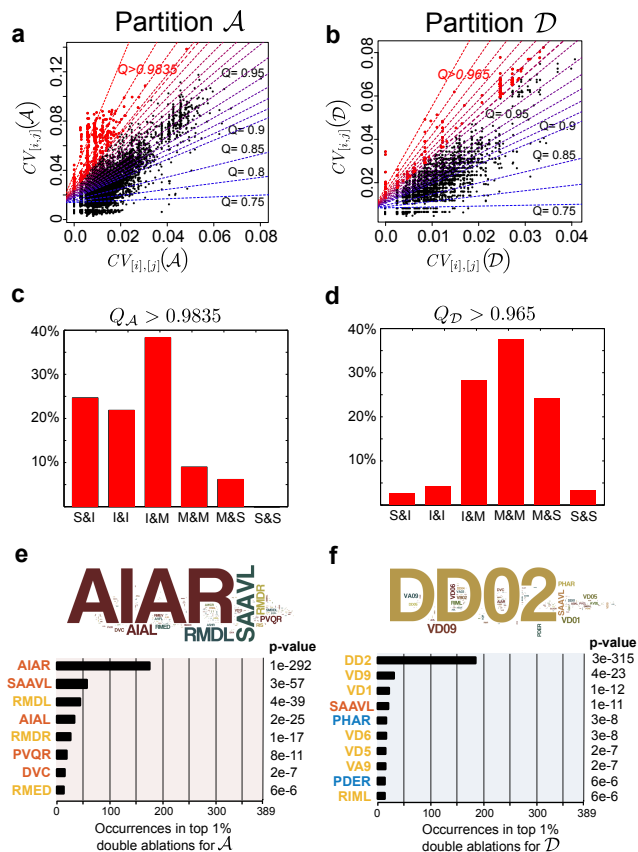


Figure 5. **Supra-additive double ablations.** The combined effect of each two neuron ablation is compared against the additive effect of the corresponding two single ablations. The results of Quantile Regression of CV of the pair against the averaged CV of the two single ablations (see Section IVD 2) are shown for: (a) Partition \mathcal{A} and (b) Partition \mathcal{D} . The top 1% pairs with the largest supra-additive effect are found above the quantile scores $Q_{\mathcal{A}} > 0.9835$ and $Q_{\mathcal{D}} > 0.965$, respectively. These top 1% double ablations are dominated by: (c) interneurons for \mathcal{A} ; (d) motor neurons for \mathcal{D} . Over-represented neurons in the top 1% supra-additive pairs for: (e) Partition \mathcal{A} , and (f) Partition \mathcal{D} . Only neurons with $p < 10^{-5}$, as calculated using a one-sided Fisher exact test, are listed. The names of the neurons are coloured according to their type: S (blue), I (red), M (yellow). The word-clouds serve as a visualisation of the computed over-representations.

(Fig. 5c-d). This observation complements the results for single ablations in Figure 4. For Partition \mathcal{A} , maximal impact of a single ablation is achieved through the deletion of motor neurons, but double ablations containing interneurons are more synergistic. For the coarser Partition \mathcal{D} , the most disruptive single ablations are those of interneurons, yet on average the most synergistically disruptive double ablations include motor neurons. Such joint effects underline the structured complexity of the connectome network and reinforce the fundamental importance of I and M neurons in the disruption of flows. In particular, the relative abundances of particular neurons in the top supra-additive pairs (Fig. 5e-f) show that in-

terneurons AIAR/L, SAAVL and PVQR and motor neurons RMDL/R are overly represented for Partition \mathcal{A} . These neurons thus have a magnifying disruptive effect for the medium scales of the connectome. For the coarser Partition \mathcal{D} , this magnifying effect on larger scales is induced mostly by motor neurons DD2, VD9, VD1 and interneuron SAAVL.

If we consider the effect on both medium and large scales, only nine double ablations appear in the top 1% for both Partition \mathcal{A} and \mathcal{D} (Table I). Interestingly, none of these pairs is linked by an edge in the connectome. Note that eight out of these nine pairs contain interneuron AIAR. The amphid interneurons AIA (along with AIB, AIY and AIZ) have a specific position in the connectome: they receive synapses from sensory neurons driving motion. Their prominent role in locomotion integration has been previously discussed and backed by *in vivo* ablation experiments [6]. Our results indicate that the deletion of pairs of neurons involving AIAR would have a particular magnifying effect on the disruption of the flow organisation at all scales of the connectome. The asymmetry observed in how the ablations of AIAL and AIAR affect the flows in the connectome is worth of further experimental investigation. The full set of outcomes of both single and double ablations are presented in the Supplementary Data as a guide for possible experimental investigations.

Table I. Double ablations within the top 1% of supra-additive pairs for both Partition \mathcal{A} and \mathcal{D} chosen according to their quantile scores ($Q_{\mathcal{A}} > 0.9835$ and $Q_{\mathcal{D}} > 0.965$).

Double ablation	Neuron types	$Q_{\mathcal{A}}$	$Q_{\mathcal{D}}$
AIAR + AQR	I & S	0.9975	0.9785
AIAR + AVEL	I & I	0.9975	0.9650
AIAR + DA2	I & M	0.9875	0.9785
AIAR + VA2	I & M	0.9945	0.9655
AIAR + VB2	I & M	0.9970	0.9785
AIAR + VD5	I & M	0.9950	0.9785
AIAR + VD6	I & M	0.9950	0.9785
AIAR + PVCR	I & I	0.9980	0.9785
SAAVL + AQR	I & S	0.9955	0.9730

C. Identifying flow roles in the directed connectome

A complementary analysis of the directed connectome of *C. elegans* is provided by the Role Based Similarity (RBS) framework [29, 30], which identifies *flow roles* for the nodes of the network without imposing *a priori* the type or number of roles. RBS evaluates the incoming and outgoing flows at each node, and identifies classes of nodes with similar in- and out-flow patterns, which we denote *flow roles*. Because they include information at all scales, flow roles capture nuanced information about

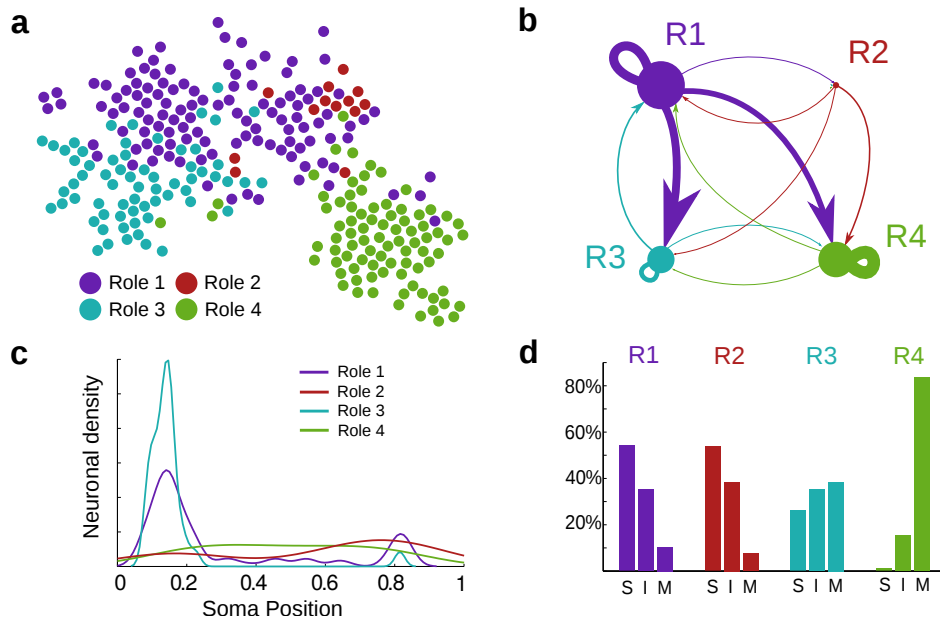


Figure 6. **Flow roles for neurons in the *C. elegans* connectome.** (a) Using RBS, we detect four flow roles in the directed connectome (see also Fig. S3 in *SI*). (b) The coarse-grained representation summarises the flow profiles of the roles: two upstream roles (R1, R2), with a dominant source character and high PageRank (Fig. S4 in *SI*), and two downstream roles (R3, R4), with a dominant sink character and lower PageRank. Yet each role has distinctive in- and out-flow patterns in relation to the others. (c) Spatial density of neurons for each role: R1 and R3 are localised predominantly in the head; R2 and R4 are spread out along the body. Note how the upstream role R2 has significant localisation in the tail. (d) The proportions of sensory (S), inter- (I) and motor neurons (M) in each role underline their functional differences.

the network, beyond pre-defined categories (e.g., sources, sinks, hubs) or combinatorial notions based on immediate neighbourhoods (e.g., social roles from Structural Equivalence [41] and Regular Equivalence [42]). Details of the RBS methodology are given in Refs. [28–31], and summarised in Section IV E and *SI* (Figs. S3 and S4).

In the *C. elegans* connectome, RBS identifies four distinct flow roles for the neurons (Fig. 6 and *SI*). When analysed in detail *a posteriori*, we find that two of the roles found (R1 and R2) have a dominant ‘source’ character (i.e., higher average in-degree than out-degree) and contain most of the nodes with high PageRank (Fig. S2 in *SI*). The other two roles (R3 and R4) have a dominant ‘sink’ character and nodes with low PageRank. Note, however, that these roles are not just defined by such average properties but by their global flow patterns in the network. As seen in Fig. 6b, R1 is upstream from R3 and R4, whereas R2 is upstream only from R4. Furthermore, R4 is an almost pure downstream module, whereas R3 has a stronger feedback connection with R1.

In particular, the RBS flow roles are linked to physiological properties of the neurons (Fig. 6c-d). R4 corresponds to a group of motor neurons (mostly ventral chord motor neurons) consistent with its downstream character, whereas R1 is a group of mostly sensory and interneurons with heavy localisation in the head. R3 is a group with a balanced representation of all three types of neurons (including some polymodal neurons) localised

in the head. Indeed, most ring neurons in R3 are in community C1, indicating a self-contained unit that process head-specific behaviour, such as foraging movements and the head withdrawal reflex [39].

Perhaps most interestingly, RBS reveals a specific flow role (R2) for a small group of neurons, mainly sensory and interneurons upstream from the motor neurons in R4. R2 contains thirteen neurons, the majority of which are responsible for escape reflexes triggered in the presence of noxious factors (Table II). Hence R2 can be seen as a group of *escape response neurons* including: the PVDL/R neurons, which sense cold temperatures and harsh touch along the body; FLPL/R, which perform the equivalent task for the anterior region; PHB neurons responsible for chemorepulsion; PHCR, which detects noxiously high temperatures in the tail; SDQL and PQR, which mediate high oxygen and CO₂ avoidance, respectively; and PLMR, a touch mechanosensor in the tail [2]. This escape response group is heavily over-connected to command neurons AVA/R, AVDL/R, DVA, PVCL/R, all of which modulate the locomotion of the worm. (Specifically, there are 48 connections from R2 to these particular command neurons in contrast to the ~12 connections expected at random.) Note that AVDL/R and DVA are in R1, whereas AVA/R and PVCL/R are in R4; the R2 group thus links directly to motor locomotion neurons across the worm. We remark that this group of neurons was found exclusively through

the analysis of their all-scale in/out flow profiles, without any other extrinsic information.

Table II. **Role 2 (R2) neurons:** The thirteen neurons identified in R2 constitute a group of *escape response neurons* containing sensory neurons responsible for modulating escape reflex reactions upon different stimuli.

Neuron(s)	Noxious factor
FLPL/R	Harsh touch, low temperature (head)
PHBL/R	Chemicals
PHCR	High temperature (tail)
PLMR	Gentle touch (tail)
PQR	CO ₂
PVDL/R	Harsh touch, low temperature
SDQL	High O ₂
SAAVL/R	No known factor
VD11	No known factor

D. Information propagation in the connectome: biological input scenarios

Despite its modest size, the nervous system of *C. elegans* can sense and react to a wide range of mechanical, chemical and thermal factors [39]. Standard notions in neuroscience hold that stimuli lead to motor action due to information progressing from sensory through inter- to motor neurons [43]. However, the underlying mechanisms and precise signal flows are still far from understood. In the absence of measurements probing such pathways, and as a first approximation to more realistic nonlinear dynamical models, we use here simplified diffusive dynamics (see Section IV B) to mimic signal propagation in the *C. elegans* directed network. Such an approach, already suggested by Varshney *et al.* [4], is naturally linked to MS multiscale community detection and to the identification of RBS flow roles, since both Markov Stability and Role Based Similarity are intrinsically defined in terms of a diffusive process on the graph.

To mimic the propagation of stimuli associated with particular biological scenarios, a normalised initial flow vector $\phi(0)$ is localised at specific input neurons and we observe the decay towards stationarity under Eq. (4):

$$\theta(t) = \phi(t) - \pi. \quad (1)$$

Initially, $\theta_i(0)$ is positive only for the input neurons where we inject the signal, and negative for all other neurons. Asymptotically, the vector of flows $\phi(t)$ approaches the stationary solution π , and $\theta_i(t) \rightarrow 0, \forall i$. For some neurons, $\theta_i(t)$ becomes positive if neuron i receives an influx of flow that drives it to ‘overshoot’ above its stationary value; other neurons approach stationarity without overshooting, depending on the particular initial input and the relative location of each neuron in the network.

We have conducted four case studies corresponding to different biological scenarios in which the input is localised on specific neurons:

- (i1) posterior mechanosensory stimulus [5, 7]: PLML/R, PVDL/R, PDEL/R
- (i2) anterior mechanosensory stimulus [5, 7]: ADEL/R, ALML/R, AQR, AVM, BDUR/L, FLPL/R, SIADL/R
- (i3) posterior chemosensory stimulus (also reported as anus mechanosensory stimulus) [7, 32]: PHAL/R, PHB/R
- (i4) anterior chemosensory stimulus [32]: ADLL/R, ASHL/R, ASKL/R.

We exemplify the procedure in detail through the posterior mechanosensory stimulus (i1), but detailed results for the other stimuli are provided in the *SI*. As shown in Figure 7a, the signal proceeds ‘downstream’ following the expected biological information processing sequence, $S \rightarrow I \rightarrow M$. The signal is initially concentrated on the input neurons (mostly sensory); then propagates out primarily to interneurons, which overshoot and peak at $t \approx 1.5$; and is then passed on to motor neurons, which slowly increase towards their stationary value.

Our flow roles provide further insight into the propagation of stimuli. As seen in Figure 7c, the input for the tail mechanosensory scenario (i1) is heavily concentrated on R2 neurons (the escape response group), from which the signal flows quickly towards the other upstream (head) group R1, followed by propagation towards the downstream group R4. Finally, the signal spreads more slowly to R3, the head-centric downstream unit. This pattern of propagation carries onto the sequence of strong response neurons (Figure 7b), and reflects the fact that R2 contains posterior upstream units, and mirrors the strong connectivity of R2 with motor neurons in R1 (AVDL/R and DVA) and R4 (PVCL/R), as discussed above.

To detect key neurons comprising the specific propagation pathways, we find *strong response neurons* (see Fig. S5 in *SI*), i.e., those with large overshoots relative to their stationary value,

$$q_{\max,i} = \max_t q_i(t) > 1 + \frac{2}{3},$$

where $q_i(t) = \phi_i(t)/\pi_i$. According to this criterion, we obtain 26 strong response neurons for scenario (i1). The neurons have large overshoots in two time windows after the initial input (Figure 7b). The details of the network propagation (Figure 7d) show that a first wave of peak responses (around $t \approx 1$) mostly corresponds to overshooting interneurons, including AVDL/R and DVA, responsible for mechanosensory integration, and PVCL/R, drivers of forward motion [5, 39]. The second wave of peaks (around $t \approx 3$) contains predominantly ventral B-type motor neurons, e.g., DB2-7 and VB11. Such B-type motor neurons are responsible for forward motion. Hence

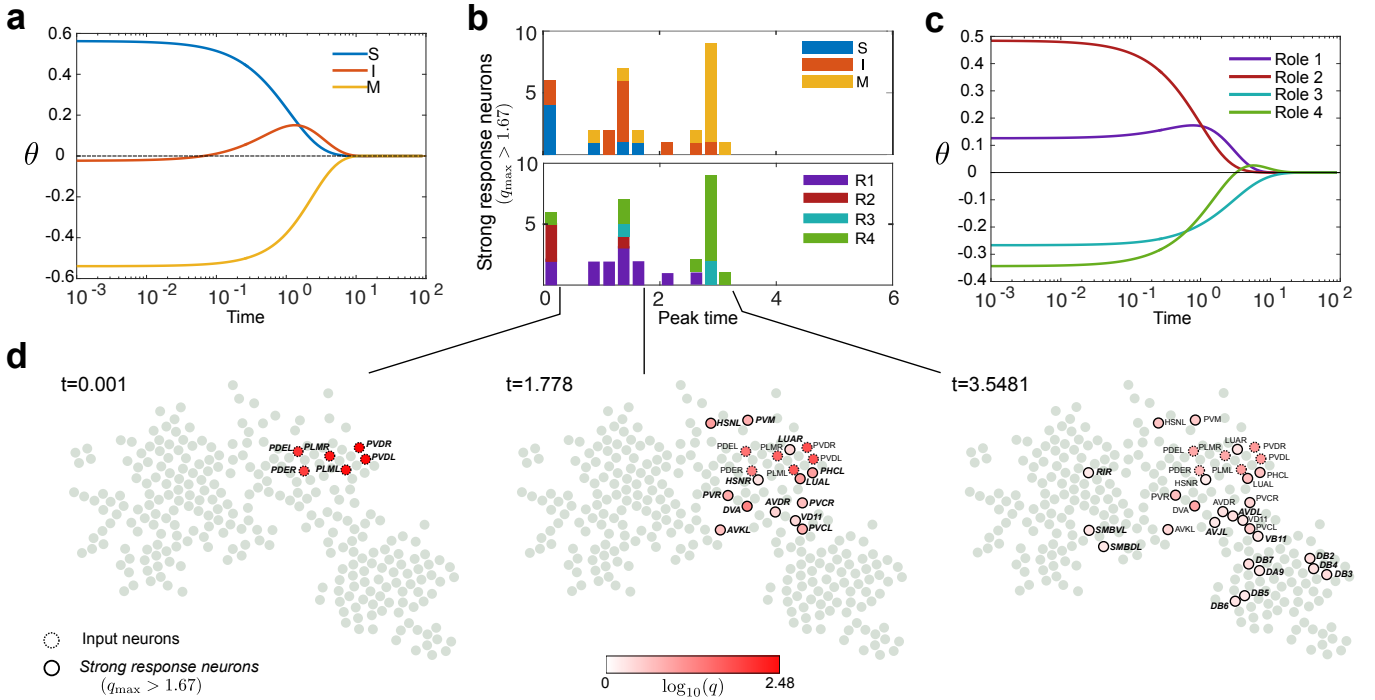


Figure 7. **Signal propagation of posterior mechanosensory stimulus (i1).** (a) As stationarity is approached ($\theta(t) \rightarrow 0$), the input propagates from sensory to motor neurons through an intermediate stage when interneurons overshoot. (b) Signal propagation as a cascade of strong response neurons (32 neurons with $q_{\max} > 1 + 2/3$) with peak times concentrated around two bursts. The number of neurons are colored according to type (top) and role (bottom). Note the overall trend $S \rightarrow I \rightarrow M$ during the propagation of strong responses, and how the sequence of strong response neurons also reflects the connectivity between roles propagating roughly from R2 to R1 and finally to R3. (c) The input (i1), which is highly localised on R2 neurons, diffuses quickly to R1 neurons and induces an overshoot of R4 neurons followed by slower diffusion into R3 neurons. (d) Stages of signal propagation in the network showing the strong response neurons that have peaked at each time.

the progression of overshooting neurons suggests a plausible biological response for a posterior mechanosensory stimulus [7, 39].

1. Comparison with other biological scenarios

Detailed results of propagation under the other biological scenarios (i2)-(i4) are presented in Figs. S6-S8 in *SI*. The overall progression of the signal from S to I to M is observed with small differences in all scenarios. However, the different scenarios exhibit distinctive participation of the flow roles. In particular, both posterior stimuli (i1) and (i3) spread from R2 neurons quickly into R1 neurons and R4 (motor) neurons, with weak propagation into R3 neurons in these two scenarios. On the other hand, anterior stimuli (i2) and (i4) spread from the R1 group strongly into R3 neurons and also quickly to R2 neurons, with only weak spreading into R4 neurons. In cases (i1)-(i3) information flows fast out of R2 towards motor neurons, as could be expected from neurons triggering an escape response. Interestingly, the (i4) scenario does not feature any strong response neurons in the R2 group. We remark that the inputs correspond to biological scenarios from the literature while our role classifica-

tion emerged from flow features of the connectome.

As shown Figs. S6-S8 in the *SI* and summarised in Fig. 8, the signal propagation pathways have distinctive characteristics for each of the scenarios. For instance, although the posterior chemosensory scenario (i3) shows strong similarities to (i1) at earlier stages (input mostly R2 and strongly responding interneurons PVCL/R, AVDL/R, AVJL, DVA), they show differences in their strong response motor neurons. In particular, for (i3) A-type neurons (DA8, DA9, VA12) responsible for backward motion are present in addition to B-type neurons (DB2, DB3, DB7).

The anterior (head) scenarios (i2) and (i4) have inputs mostly localised on R1, which diffuse towards the head-centric group R3 instead of R4. In fact, in case (i4) we do not even observe overshooting among ventral cord motor neurons present in all other cases. For the anterior mechanosensory scenarios (i2), command interneurons such as PVCL/R, AVDL/R respond strongly, together with ring interneurons, such as RIGL/R and RIBL/R. In this case, only small excitation of ventral cord motor neurons is attained; instead, we observe strong response of polymodal ring motor neurons, such as URADL/R and SIADL/R. Interestingly, sensory neurons CEPVL/R and CEPDL/R also respond strongly, even

though they receive no external input. CEP neurons are reported to be functionally redundant with nose touch receptors ADE where the input signal was placed [39]. Upon anterior chemical stimulation (i4), a bulk of flow is captured within the neuronal ring and induces strong response from chemosensory neurons such as PVQL, ASKL, AWAL/R, AWABL/R and AWACL/R, as well as interneurons RICL/R, RMGL/R, AIAL/R and AIBL/R, which are specific for integrating chemo-sensation. Several of these neurons appear in the posterior chemosensory stimulus (i3) too. Role-wise, the head-centric downstream R3 neurons are strongly active under scenario (i4), yet the R4 ventral cord neurons remain largely quiescent. A summary of the strong response and overshooting neurons for all scenarios is presented in Figure 8.

III. DISCUSSION

We have presented an integrated network-theoretic analysis of the *C. elegans* connectome in terms of directed flows. We exploit the connection between diffusive processes and graph-theoretical properties, which intimately link structure and dynamics, to elucidate dynamically relevant features in the connectome. Although diffusive processes are a coarse approximation of physiological signal propagation, they can be used to extract systemic features of dynamical relevance, specifically in the case of non-spiking neuronal systems such as *C. elegans* [4].

Using the Markov Stability framework, we have identified flow-retaining groupings of neurons in the *C. elegans* connectome at different levels of granularity. Previous studies [20–22] have aimed at uncovering modules based on structural properties of the network, usually considering a particular scale so as to find just one partition. (In the *SI* we provide a detailed comparison of MS multiscale flow structures against partitions found by Modularity [20, 21], stochastic block models [22] and MapEquation [44].) In contrast, MS provides a multiscale description across all scales by sweeping the Markov time [27], respecting and exploiting directionality. In doing so, it reveals an intrinsic, quasi-hierarchical organisation of the connectome, giving insight into relevant features of signal propagation. The partitions found by MS are in good agreement with current knowledge of *C. elegans* physiology, and summarise previously observed features of the *C. elegans* connectome, such as the hierarchical and spatial organisation of neuronal communities [23, 34].

In addition, the flow structure identified by MS highlights the prominent position of particular neurons, such as AVF and AVH, and allows for a systematic exploration of the single and double ablations that are most disruptive of signal flows. This framework provides insight into candidate neurons for further experimental investigations, such as the synergistic effects caused by neuron AIAR in double ablations, or the global role of D-type motor neurons, which often appear as relevant in sin-

gle ablations. Although little is known about the specific role of the polymodal (I/M) SAAVL/R head neurons [39], these neurons appear in the R2 group and are salient in our ablations, suggesting them as good candidates for further investigation.

Using Role Based Similarity, we identify roles that neurons play with respect to flows in the *C. elegans* nervous system. RBS reveals two groups of upstream neurons and two groups of downstream neurons, with a specific inter-connectivity pattern. Previous studies have assigned roles following pre-defined classifications [45] or by exploring the core-periphery structure [46]. In contrast, RBS extracts roles according to features of incoming and outgoing flow patterns at all scales. The nuanced use of network flows enables us to go beyond standard classifications [28, 31], e.g. centrality scores or combinatorial notions of neighbourhood as in regular and structural equivalence. (See *SI* for a comparison of RBS and regular equivalence.) In particular, our RBS analysis singles out a small group of upstream neurons (R2), which is functionally linked to escape responses from noxious factors and could be the object of further investigation.

The RBS roles are also informative of the specific features of signal propagation of different ‘input-response’ *in silico* experiments motivated by biological scenarios (see Fig. S9 in the *SI*). In particular, the R2 group plays an important role in the propagation of biological stimuli, especially posterior, channelling stronger and faster responses, whereas the downstream, head-centric R3 group constitutes a self-contained grouping, mainly accessible via the upstream, head-centric R1 group. The distinctive propagation profiles obtained for the different biological scenarios suggest that the graded organisation of the nodes in terms of upstream-downstream information distribution could provide valuable insight into functional circuits and responses.

Such computational tools could be used in conjunction with experimental techniques, and aid in the generation of functional hypotheses for experimental evaluation, with the eventual aim of linking wiring properties of the connectome with information processing and functional behaviour. Interesting extensions of theoretical interest would also include considering the *C. elegans* connectome as a multiplex network, taking into account the different types of synapse in a more explicit fashion, and enriching the dynamics of the model by incorporating the inhibitory character of GABA-ergic synapses and nonlinearities in the dynamics.

IV. MATERIALS & METHODS

A. The *C. elegans* neuronal network

The information of the large component of the connectome network is encoded into the $n \times n$ adjacency matrix A ($n = 279$), where entry A_{ij} counts the total number of synapses (both chemical synapses and gap junctions)

matrix defined as follows:

$$M = \tau D^\dagger A + \frac{1}{n} [(1 - \tau) \mathbf{1} + \tau \mathbb{1}_{d_i=0}] \mathbf{1}^T. \quad (3)$$

Here, $\tau \in (0, 1)$ is the Google teleportation parameter (and we take $\tau = 0.85$ as is customary in the literature); $\mathbb{1}_{d_i=0}$ is the indicator vector of sink nodes; and the diagonal matrix D^\dagger is the pseudo-inverse of the degree matrix:

$$D_{ii}^\dagger = \begin{cases} 0 & \text{if } d_i = 0 \\ 1/d_i & \text{if } d_i \neq 0. \end{cases}$$

The matrix M describes a signal diffusion along the directed edges with an additional re-injection of external ‘environmental noise’: each node receives inputs from its neighbours (which transmit flow along their outgoing links according to their relative weight with probability τ) and receives a constant external re-injection of size $(1 - \tau)/n$. For pure sinks, the outgoing flow is uniformly redistributed to all nodes so as to avoid the signal accumulating at nodes with no out-links. Mathematically, this reinjection of probability (known as teleportation in the networks literature) guarantees the existence of a unique stationary solution for Eq. (2), even when the network is not strongly connected [26, 52]. Biophysically, the teleportation can be understood as modelling the random interactions with the external environment.

Let $\phi(0)$ be the input, i.e., the signal at $t = 0$. The solution of Eq. (2) is then:

$$\phi(t) = \phi(0) \exp(t[M - I]), \quad (4)$$

with stationary solution $\phi(t \rightarrow \infty) = (\phi(0) \cdot \mathbf{1}) \boldsymbol{\pi}$, where $\boldsymbol{\pi}$ is the dominant left eigenvector of M , known as PageRank [52]. Therefore, under a unit-normalised input, $\phi(t) \cdot \mathbf{1} = 1 \forall t$, and the stationary solution is $\boldsymbol{\pi}$.

C. A dynamical perspective for community detection in graphs: Markov Stability

The diffusive dynamics (2) can be exploited to reveal the multiscale organisation of the *C. elegans* connectome using the Markov Stability community detection framework [24–26]. Markov Stability finds communities across scales by optimising a cost function related to this diffusion (parametrically dependent on time) over the space of all partitions.

More formally, a partition \mathcal{P} of the n nodes of the network into m non-overlapping communities is encoded as a $n \times m$ indicator matrix $H_{\mathcal{P}}$:

$$[H_{\mathcal{P}}]_{ic} = \begin{cases} 1 & \text{if node } i \text{ belongs to community } c \\ 0 & \text{otherwise.} \end{cases} \quad (5)$$

Given a partition matrix $H_{\mathcal{P}}$, we define the time-dependent clustered autocovariance matrix:

$$R(t, H_{\mathcal{P}}) = H_{\mathcal{P}}^T [\Pi \exp(t[M - I]) - \boldsymbol{\pi} \boldsymbol{\pi}^T] H_{\mathcal{P}}, \quad (6)$$

where $\Pi = \text{diag}(\boldsymbol{\pi})$. The matrix entry $[R(t, H_{\mathcal{P}})]_{cf}$ quantifies how likely it is that a random walker starting in community c will end in community f at time t , minus the probability for such an event to happen by chance. To find groups of nodes where flows are trapped more strongly over time t than one would expect at random, we find a partition \mathcal{P} that maximises

$$r(t, H_{\mathcal{P}}) = \text{trace } R(t, H_{\mathcal{P}}). \quad (7)$$

We define $r(t, H_{\mathcal{P}})$ as the *Markov Stability* of partition \mathcal{P} at time t [24, 26].

Maximising $r(t, H_{\mathcal{P}})$ over the space of all partitions for each time t results in the sequence of optimal partitions:

$$\mathcal{P}_{\max}(t) = \arg \max_{\mathcal{P}} r(t, H_{\mathcal{P}}). \quad (8)$$

Although the optimisation (8) is NP-hard, there exist efficient heuristic algorithms that work well in practice. In particular, it has been shown that this optimisation can be carried out using any algorithm devised for modularity maximisation [24–26]. In this work, we use the Louvain algorithm [53], which is known to offer high quality solutions whilst remaining computationally efficient.

As an additional improvement of the optimisation of $\mathcal{P}_{\max}(t)$, we run the Louvain algorithm $\ell = 100$ times with different random initialisations for each Markov time t , and generate an ensemble of solutions $\{\mathcal{P}_i(t)\}_{i=1}^{\ell}$. From this ensemble, we pick the best partition $\widehat{\mathcal{P}}(t)$ according to our measure (7):

$$\max_i \{\mathcal{P}_i(t)\}_{i=1}^{\ell} \mapsto \widehat{\mathcal{P}}(t) \approx \mathcal{P}_{\max}(t).$$

Ideally, the optimised partition from the ensemble, $\widehat{\mathcal{P}}(t)$, will be close to the true optimum, $\mathcal{P}_{\max}(t)$.

To identify the important partitions across time, we use the following two robustness criteria [27, 54]:

a. Consistency of the optimised partition: A relevant partition should be a robust outcome of the optimisation, i.e., the ensemble of ℓ optimised solutions should be similar. To assess this consistency, we employ an information-theoretical distance between partitions: the normalised variation of information between two partitions \mathcal{P} and \mathcal{P}' defined as [55]:

$$VI(\mathcal{P}, \mathcal{P}') = \frac{2\Omega(\mathcal{P}, \mathcal{P}') - \Omega(\mathcal{P}) - \Omega(\mathcal{P}')}{\log(n)}, \quad (9)$$

where $\Omega(\mathcal{P}) = -\sum_{\mathcal{C}} p(\mathcal{C}) \log p(\mathcal{C})$ is a Shannon entropy, with $p(\mathcal{C})$ given by the relative frequency of finding a node in community \mathcal{C} in partition \mathcal{P} ; $\Omega(\mathcal{P}, \mathcal{P}')$ is the Shannon entropy of the joint probability; and the factor $\log(n)$ ensures that the measure is normalised between [0, 1].

To quantify the robustness to the optimisation, we compute the average variation of information of the ensemble of solutions obtained from the ℓ Louvain runs at Markov time t :

$$\langle VI(t) \rangle = \frac{1}{\ell(\ell - 1)} \sum_{i \neq j} VI(\mathcal{P}_i(t), \mathcal{P}_j(t)). \quad (10)$$

If all runs of the optimisation return very similar partitions, then $\langle VI(t) \rangle$ will be small, indicating robustness of the partition to the optimisation. Hence we select partitions with low values (or dips) of $\langle VI(t) \rangle$.

b. Persistence of the partition over time: Relevant partitions should also be optimal across stretches of Markov time. Such persistence is indicated by a plateau in the number of communities over time and by a low value plateau of the cross-time variation of information:

$$VI(t, t') = VI(\widehat{\mathcal{P}}(t), \widehat{\mathcal{P}}(t')). \quad (11)$$

D. Quantifying the disruption of community structure under node deletion

To mimic *in silico* the ablation of neuron i , we remove the i -th row and column of the adjacency matrix A , and analyse the change induced in the Markov Stability community structure of the reduced $(n-1) \times (n-1)$ matrix $A_{[i]}$. Double ablations are mimicked by simultaneously removing two rows (and their corresponding columns) to obtain the reduced $(n-2) \times (n-2)$ matrix $A_{[i,j]}$.

1. Detecting salient single-node deletions

We carry out a systematic study of all single node deletions in the network. To detect relevant deletions, we monitor either an induced loss of robustness or an induced disruption in the make-up of particular partitions.

a. Changes induced in the robustness of partitions: First, we run the MS analysis on *all* deletions to obtain the optimised partitions and their robustness across all times t :

$$\left\{ \widehat{\mathcal{P}}_{[i]}(t), \langle VI_{[i]}(t) \rangle \right\}_{i=1}^n \quad \forall t. \quad (12)$$

We then fit a Gaussian Process (GP) [56] to the ensemble of $n+1$ time series of the robustness measure $\langle VI_{[i]}(t) \rangle$, plus the unablated $\langle VI(t) \rangle$. The resulting GP, with mean $\mu(t)$ and variance $\sigma^2(t)$, describes the average robustness of partitions under a single-node deletion.

To detect single-node deletions that induce a large change in the robustness of a given partition we find sustained outliers of the GP. For a partition $\widehat{\mathcal{P}}$ optimal over $t \in [t_1, t_2]$, we select node deletions i such that $\langle VI_{[i]}(t) \rangle$ differs from $\mu(t)$ by at least two standard deviations $\sigma(t)$ over a continuous time interval larger than $\ln(\sqrt{t_2/t_1})$ [54]. This criterion identifies node deletions that disrupt the robustness of a partition over its epoch.

b. Changes induced in the make-up of partitions: To detect if the deletion of node i induces a change in the make-up of partition $\widehat{\mathcal{P}}$, we compute the *community variation*:

$$CV_{[i]}(\widehat{\mathcal{P}}) = \min_{\tau} VI(\widehat{\mathcal{P}}, \widehat{\mathcal{P}}_{[i]}(\tau)), \quad (13)$$

i.e., the variation of information between $\widehat{\mathcal{P}}$ and the most similar among *all* optimal partitions of the ablated network $\widehat{\mathcal{P}}_{[i]}(t)$.

We detect outliers in CV for each partition using a simple criterion based on the inter-percentile range: the deletion of i is considered an outlier if $CV_{[i]} > P_{90} + IPR_{90/10}$, where P_{90} is the 90th percentile, and $IPR_{90/10} = |P_{90} - P_{10}|$ is the interpercentile range between the 10th-90th percentiles of the ensemble of $CV_{[i]}$.

2. Detecting supra-additive double-node deletions

We have carried out a study of all double deletions in the network to detect two-node deletions whose effect is larger than the additive effect of the two corresponding single node deletions. To this end, we first obtain the set of MS partitions across all Markov times for all double deletions $\widehat{\mathcal{P}}_{[i,j]}(t)$, and compute their community variation:

$$CV_{[i,j]}(\widehat{\mathcal{P}}) = \min_{\tau} VI(\widehat{\mathcal{P}}, \widehat{\mathcal{P}}_{[i,j]}(\tau)). \quad (14)$$

We then compute the average of the individual ablations:

$$CV_{[i],[j]}(\widehat{\mathcal{P}}) = \frac{CV_{[i]}(\widehat{\mathcal{P}}) + CV_{[j]}(\widehat{\mathcal{P}})}{2}. \quad (15)$$

To find pairs with supra-additive effect, we use Quantile Regression (QR) [57], a method widely used in econometrics, ecology, and medical statistics to estimate conditional quantile functions. For a partition $\widehat{\mathcal{P}}$, we employ QR to fit quantiles for the regression of $CV_{[i,j]}(\widehat{\mathcal{P}})$ against $CV_{[i],[j]}(\widehat{\mathcal{P}})$, using all 38781 two-node ablations (Fig. 5). We report the top 1% double deletions according to their quantile scores—this is our criterion to select double-ablations that have a strong effect. All scores are computed using Bayesian Quantile Regression, as implemented in the R package `BSquare` (<https://cran.r-project.org/web/packages/BSquare/index.html>), which fits all quantiles simultaneously resulting in a more coherent estimate [58]. Following Ref. [58], we fit the quantiles to the normalised (15) using a Gamma centering distribution and four basis functions.

E. Finding flow roles in networks: Role-Based Similarity

In directed networks, nodes can have different ‘roles’, e.g., sinks, sources or hubs. In complex directed networks, functional roles may not fall into such simple categories, yet nodes can still be characterised by their contribution to the diffusion of in- and out-flows. Here we use a recent method (Role-Based Similarity, RBS) to uncover roles in directed networks based on the patterns of incoming and outgoing flows at all scales [29, 30]. The

main idea underpinning RBS is that nodes with a similar in/out flow profile play a similar role, regardless of whether they are near or far apart in the network. Each node is associated with a feature vector \mathbf{x}_i containing a weighted number of in- and out-paths of increasing lengths beginning and ending at the node. The feature vectors are collected in the feature matrix X :

$$X = \begin{bmatrix} \mathbf{x}_1 \\ \vdots \\ \mathbf{x}_n \end{bmatrix} = \left[\overbrace{\dots (\beta A^T)^k \mathbf{1} \dots}^{\text{paths in}} \mid \overbrace{\dots (\beta A)^k \mathbf{1} \dots}^{\text{paths out}} \right], \quad (16)$$

where $\beta = \alpha/\lambda_1$, with λ_1 the spectral radius of the adjacency matrix A and $\alpha \in (0, 1)$. The cosine between feature vectors gives the similarity score between nodes:

$$Y_{ij} = \frac{\mathbf{x}_i \mathbf{x}_j^T}{\|\mathbf{x}_i\|_2 \|\mathbf{x}_j\|_2}. \quad (17)$$

The $n \times n$ matrix Y quantifies how similar the directed flow profiles between every pair of nodes are. Nodes with identical connectivity have $Y_{ij} = 1$, whereas in the case of nodes with dissimilar flow profiles (e.g., if i is a source node with no incoming connections and j is a sink node with no outgoing connections), then their feature vectors are orthogonal and $Y_{ij} = 0$.

As outlined in Refs. [29–31], we compute the similarity matrix Y iteratively with $\alpha = 0.95$, and apply the RMST algorithm to obtain a *similarity graph*, in which only the important information of Y is retained. We then extract *flow roles* in a data-driven manner without imposing the number of roles *a priori* by clustering

the similarity graph (see Fig. S3 in the *SI*). The flow roles so obtained have been shown to capture relevant features in complex networks, where other role classifications based on combinatorial concepts and neighbourhoods fail [28, 31]. In particular, our flow roles are fundamentally different from notions of roles in social networks based on Structural Equivalence [41] and Regular Equivalence [42]. Such equivalence measures do not incorporate information about the large scales of the network and are sensitive to small perturbations, making them unsuitable for complex networks such as the *C. elegans* connectome [28] (see Fig. S4 in *SI* for roles based on Regular Equivalence).

Acknowledgements

KAB acknowledges an Award from the Imperial College Undergraduate Research Opportunities Programme (UROP). MTS acknowledges support from the ARC and the Belgium network DYSCO (Dynamical Systems, Control and Optimisation). YNB acknowledges support from the G. Harold and Leila Y. Mathers Foundation. MB acknowledges support from the James S. McDonnell Foundation Postdoctoral Program in Complexity Science/Complex Systems Fellowship Award (#220020349-CS/PD Fellow). MB acknowledges support from EPSRC grant EP/I017267/1 under the Mathematics Underpinning the Digital Economy program.

SUPPLEMENTARY INFORMATION

S1. MULTISCALE COMMUNITY STRUCTURE OF THE *C. ELEGANS* CONNECTOME WITH MARKOV STABILITY

Full scan of Markov times: Figure S1 displays the full MS analysis of the *C. elegans* connectome, from the finest to the coarsest scales. The analysis in the main text concentrates on the medium to coarse partitions $\mathcal{A} - \mathcal{E}$.

Quasi-hierarchical character of partitions: Figure S2 shows the conditional entropy of the partitions found by MS. The normalized conditional entropy $\Omega(\mathcal{P}(t')|\mathcal{P}(t))/\log(n) \in [0, 1]$ quantifies how much uncertainty there is about the community assignment in $\mathcal{P}(t')$, given the known partition $\mathcal{P}(t)$. If partition $\mathcal{P}(t')$ can be predicted from $\mathcal{P}(t)$, i.e. if $\mathcal{P}(t')$ is a strictly hierarchical agglomeration of the communities of $\mathcal{P}(t)$, then the conditional entropy will be zero. As seen in Figure S2, $\Omega(\mathcal{P}(t')|\mathcal{P}(t))/\log(n)$ has a strong upper-triangular character, implying that the communities are almost hierarchical.

Comparison with other partitions: The flow-based MS partitions obtained here are distinct from partitions obtained by several other methods. In particular, we have compared against partitions obtained with Modularity, Stochastic Block models, and Infomap.

Modularity has been used to obtain optimised partitions in Refs. [20, 21].

The partition found in Ref. [20] is closest to our 4-way Partition \mathcal{B} ($VI = 0.185$), whereas the partition found in Ref. [21] is closest to our 3-way Partition \mathcal{C} ($VI = 0.186$). Modularity optimisation imposes a particular intrinsic scale (or resolution) to the partition, so that partitions found with modularity are well matched to a particular scale (i.e., a particular Markov time) in the Markov Stability framework, as shown previously [24, 26]. On the other hand, as discussed in the main text, the Markov Stability framework is based on a systematic scanning across Markov times [27] allowing the intrinsic multiscale organisation to become apparent.

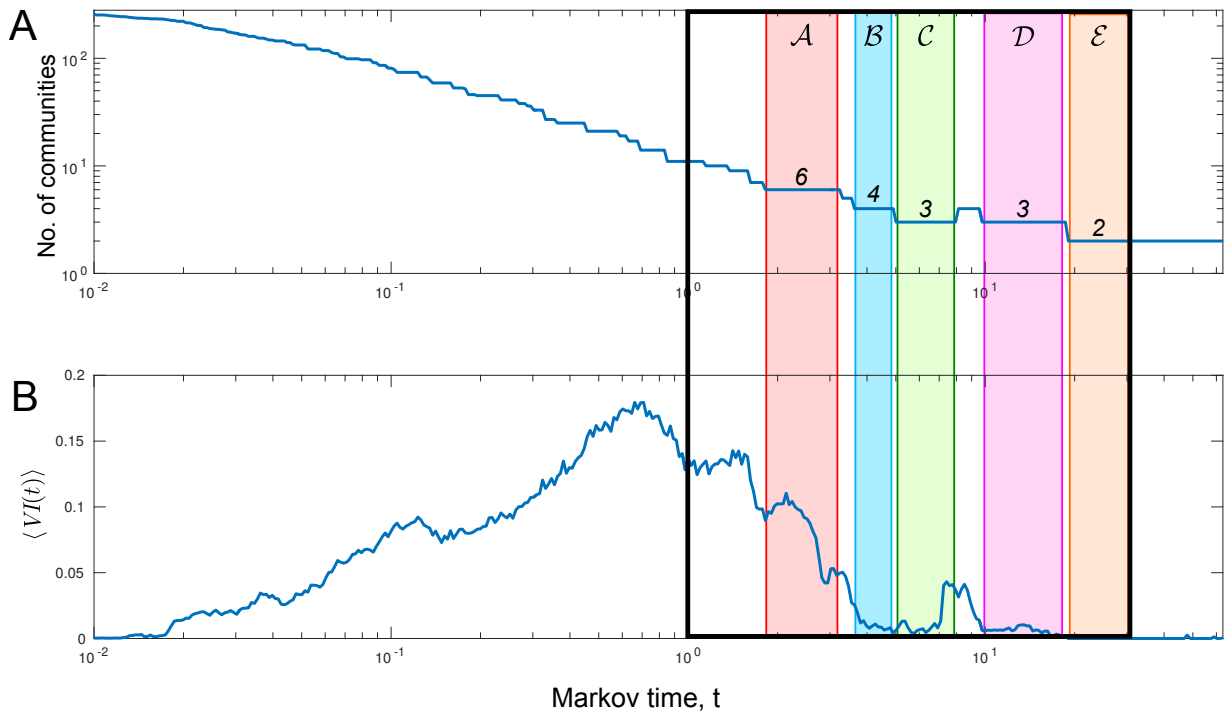


Figure S1. Full analysis with Markov Stability (MS) across all Markov times, from the finest possible partition (every node in its own partition) at small Markov times to the bipartition at large Markov times. The highlighted time interval corresponds to Fig. 1 in the main text (Fig. 1), which focusses on the medium to coarse scales.

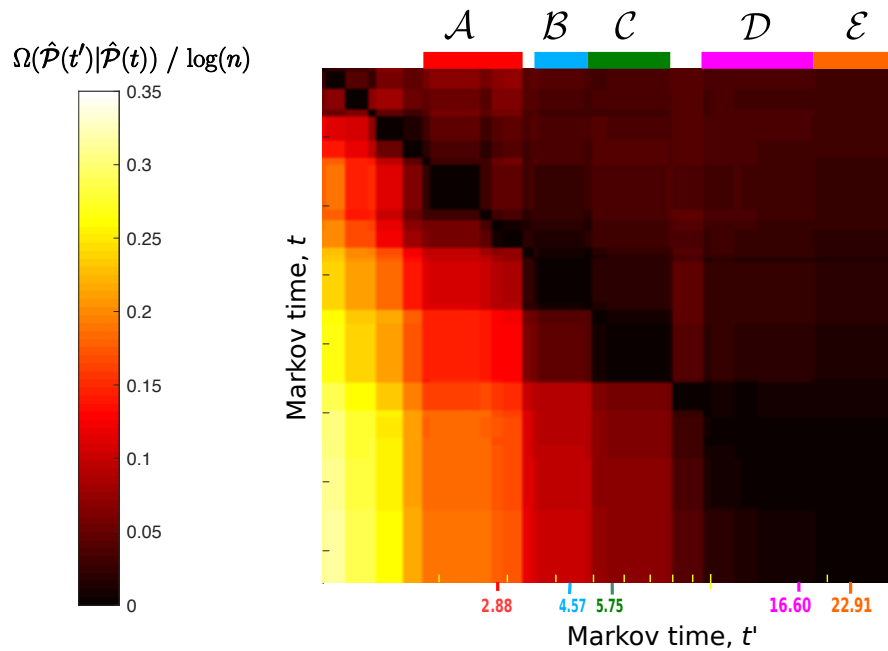


Figure S2. Normalised conditional entropy of the optimised MS partitions $\mathcal{A} - \mathcal{E}$. The observed asymmetry in this measure implies a quasi-hierarchical organisation (see text).

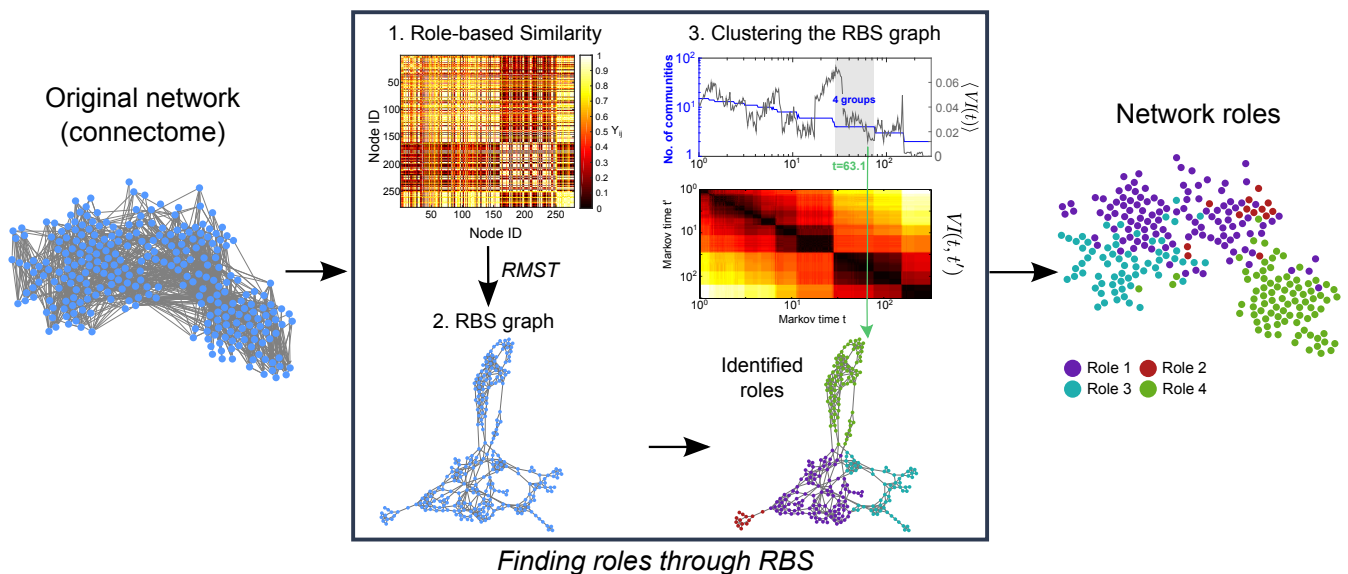


Figure S3. Role extraction with RBS, RMST, and Markov Stability. Left to right: From the original *directed* network of the *C. elegans* connectome we obtain a similarity matrix using the RBS metric. This similarity matrix is transformed into a similarity matrix using the RMST method. When Markov Stability is applied to the similarity graph, we find a robust partition into four communities, corresponding to four *flow roles*. The roles are then shown on the original connectome layout.

The partitions based on stochastic block models [22] and hierarchical Infomap [44] are less similar to the ones found by MS: the partition found by stochastic block models in [22] is closest to our 3-way Partition \mathcal{C} (but with a higher $VI=0.272$), and the partition found by hierarchical Infomap in [44] is closest to our 6-way Partition \mathcal{A} (yet with an even higher $VI=0.282$). These differences in the outcomes are expected due to the contrasting methodological approaches. In particular, Infomap is known to impose a clique-like structure to the modules leading to groupings where strong local density is favoured [59].

S2. ROLES OF NODES: THE RBS FRAMEWORK

Extracting flow roles in directed networks using RBS: Figure S3 summarises schematically the procedure to obtain flow roles using RBS analysis, as discussed in detail in [31]. First, a similarity network is created by computing a similarity score between each node in the network, based on their incoming and outgoing path-profiles, as described in the main text. Second, a similarity graph is obtained using the RMST method, which subsequently prunes out uninformative links (see Ref. [31] for details). Third, the resulting similarity graph is clustered using MS to obtain relevant groups of nodes that have similar in- and out-flow profiles at all scales.

Comparison with other analyses of roles: Our *flow roles* are fundamentally different from notions of roles used in social networks based on Structural Equivalence (SE) [41], and Regular Equivalence (RE) [42]. Figure S4 presents the comparison of our RBS roles versus those obtained based on RE by the REGE algorithm [60] (see also the Supplementary Data). Because both RE and SE consider only one-step neighbourhoods and do not incorporate information about the long scales of the network [27], they are less applicable to complex networks such as the *C. elegans* connectome [28]. In particular the roles produced by REGE show undifferentiated PageRank and connectivity profiles.

In Refs. [20, 21], roles were assigned to neurons according to the technique proposed by Guimera et al [45], identifying certain interneurons as relevant hubs between predefined communities. In Ref. [20] command interneurons (e.g. AVA, AVB, AVD, PVC) play the role of global hubs, whereas D-type motor neurons play the role of provincial hubs. These features are in line of our ablation results, where D-type motor neuron ablations alter flows at finer scales and ablation of interneurons modifies flow patterns at larger scales.

Chatterjee and Sinha [46] explored the core-periphery structure of the *C. elegans* connectome using a k -core decomposition based on in- and out- degree separately. The k -core of a network is the subgraph with the property that all nodes have (in/out)degree at least k . As expected, motor neurons are overrepresented in the k -cores based on in-degree, and sensory neurons are overrepresented in k -cores based on out-degree. This distinction between neurons with upstream and downstream roles is also an inherent characteristic in the RBS analysis, yet from a different per-

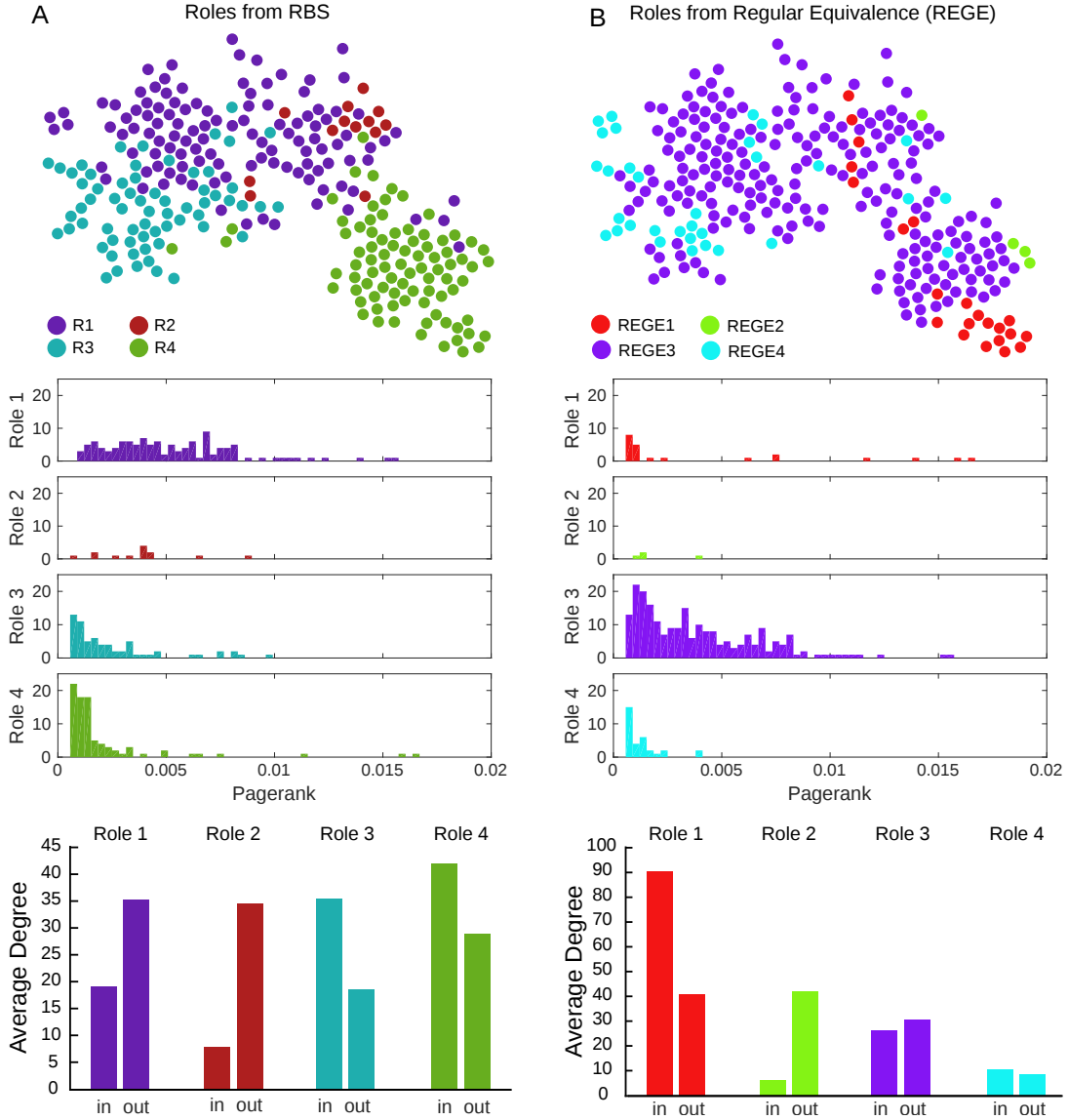


Figure S4. **A:** Roles of the nodes according to RBS with the PageRank distribution for each role and the average in/out degree for each role. **B:** Same for the roles obtained according to Regular Equivalence obtained using the REGE algorithm [60].

spective, i.e., based on the global characteristics of a node with respect to the in- and out-flows in the network, rather than based on its local connections.

S3. STYLISED SIGNAL PROPAGATION ANALYSIS

Summarising signal propagation: Signal propagation analysis can be analysed from different angles. In Figure S5, we explain concisely our approach to detect pathways of signal flow exemplified on scenario (i1).

For all neurons, we compute the time series $\phi_i(t)$, i.e., the amount of signal present at the node at Markov time t . With increasing time the amount of signal at each node will converge to its stationary value ($\theta_i(t) = \phi(t) - \pi_i \rightarrow 0$). The approach to stationarity can happen in two ways: i) the initially negative $\theta_i(t)$ approaches 0 from below; ii) $\theta_i(t)$ 'overshoots', i.e. exceeds its stationary temporarily before decaying towards its stationary value. We define the relative amount of signal with respect to the stationary value as $q_i(t) = \phi(t)/\pi_i$. We focus on nodes that have overshoot above their stationary value π_i , i.e., those with $q_{\max} := \max_t \phi_i(t)/\pi_i > 1$, and we collect the times at which they reach their peak. To summarise the signal propagation more concisely, we focus on *strong response neurons* that present a large overshoot, i.e., $q_{\max} > 5/3$, and collect the peak times. The peak-time histogram and

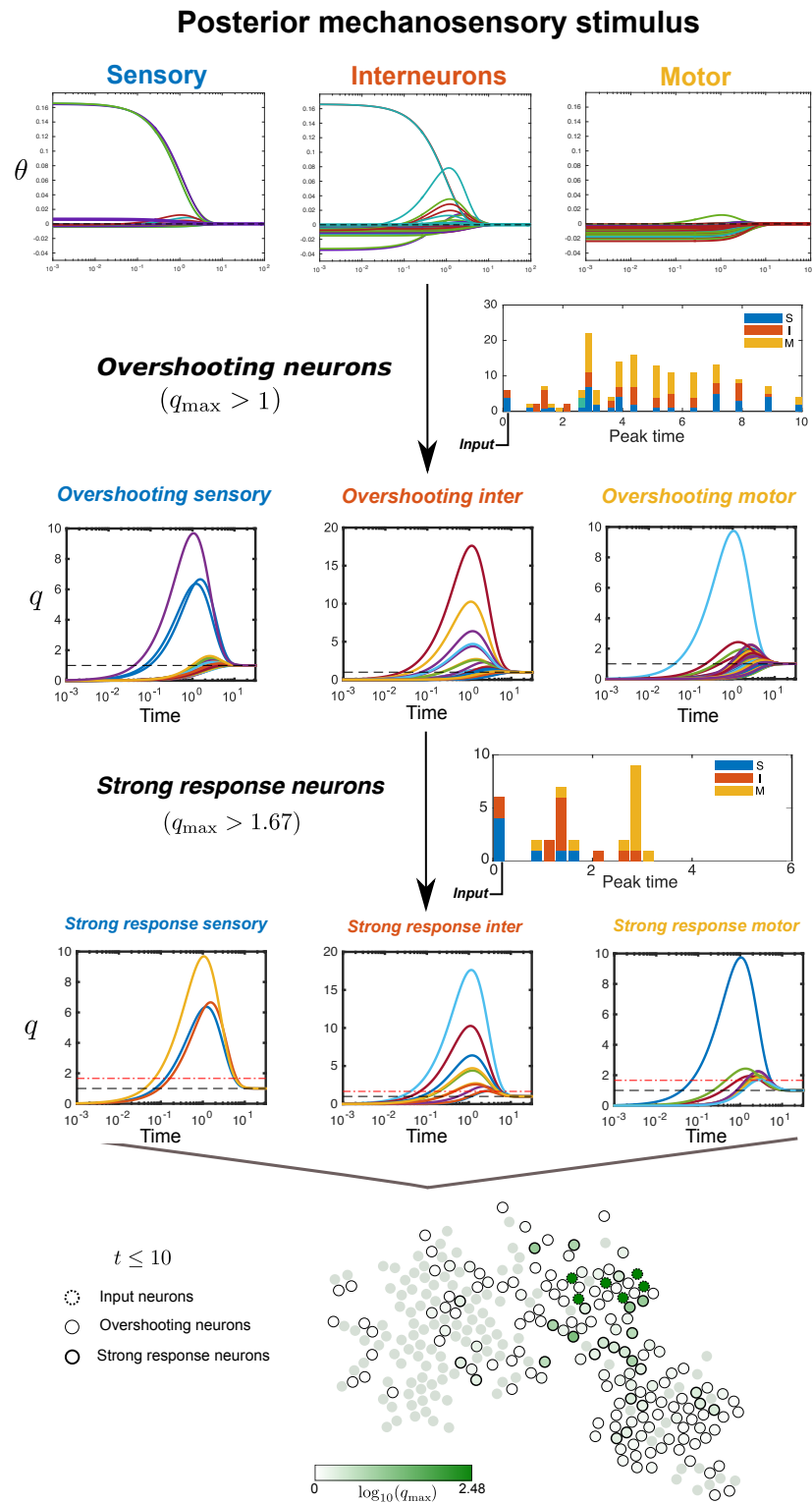


Figure S5. Operational procedure of signal propagation analysis (see text).

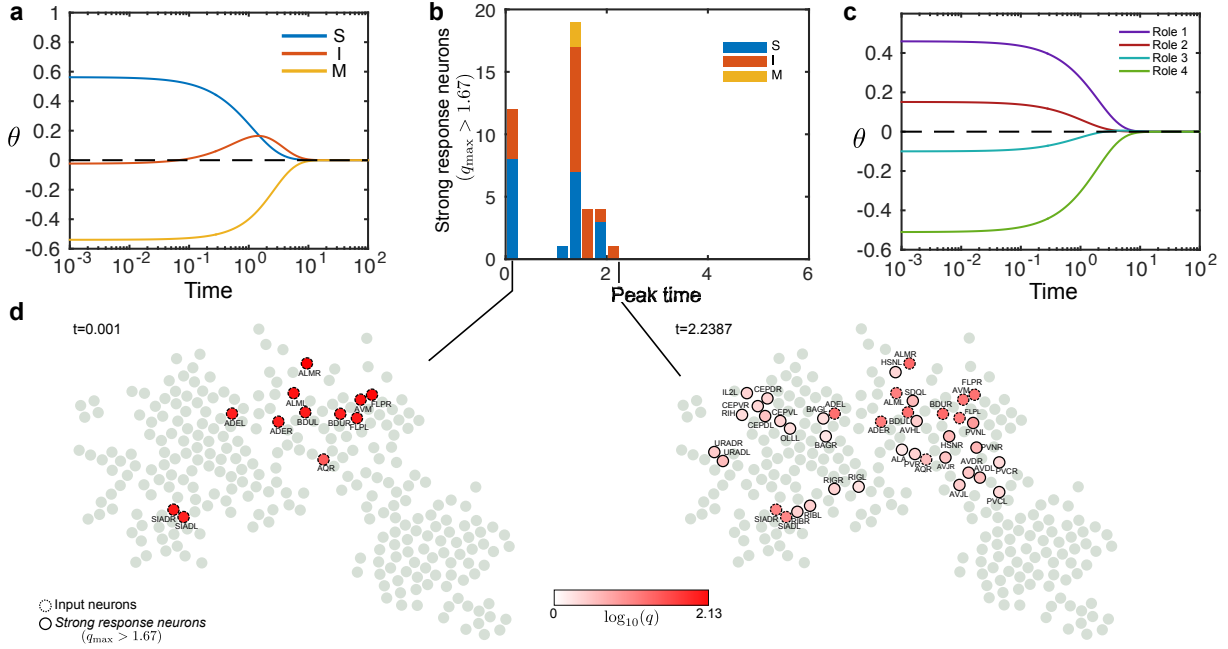


Figure S6. **Signal propagation: anterior mechanosensory stimulus (i2).** Signal propagation evolving from an initial condition localised at the mechanosensory neurons (i2). (a) As stationarity is approached ($\theta(t) \rightarrow 0$), the input propagates from sensory to motor neurons through an intermediate stage when interneurons overshoot. (b) The propagation seen as a cascade of strong response neurons ($q_{\max} > 1 + 2/3$) with peak times concentrated around two bursts. (c) The input (i2), appears localised on R1 and to a lesser extent R2 neurons. The signal diffuses somewhat quicker out of R2 than R1 neurons, but induces not collective overshoot of R3 or R4 neurons. (d) Stages of signal propagation in the network showing the strong response neurons that have peaked at each time.

the particular sequence of strong response neurons is used to characterise the different input-response biological scenarios. Analyses by neuron type and by role groups is also carried out. See Figure S5 for an illustration of these steps applied to the biological scenario (i1), corresponding to the posterior mechanosensory stimulus.

Comparison of signal propagation for the different biological scenarios: Figures S6, S7, and S8 summarise the signal propagation results for the input-response case studies (i2)-(i4), in the same way as done in Figure 7 in the main text.

Figure S9 provides a comparison of the histograms of peak times for the strong response neurons in the four biological scenarios from the perspective of flow roles. Note how the tail inputs induce strong responses on neurons spreading from R2 to R1 and finally R4. On the other hand, the head inputs induce strong responses on neurons heavily based on R1 spreading only to R3.

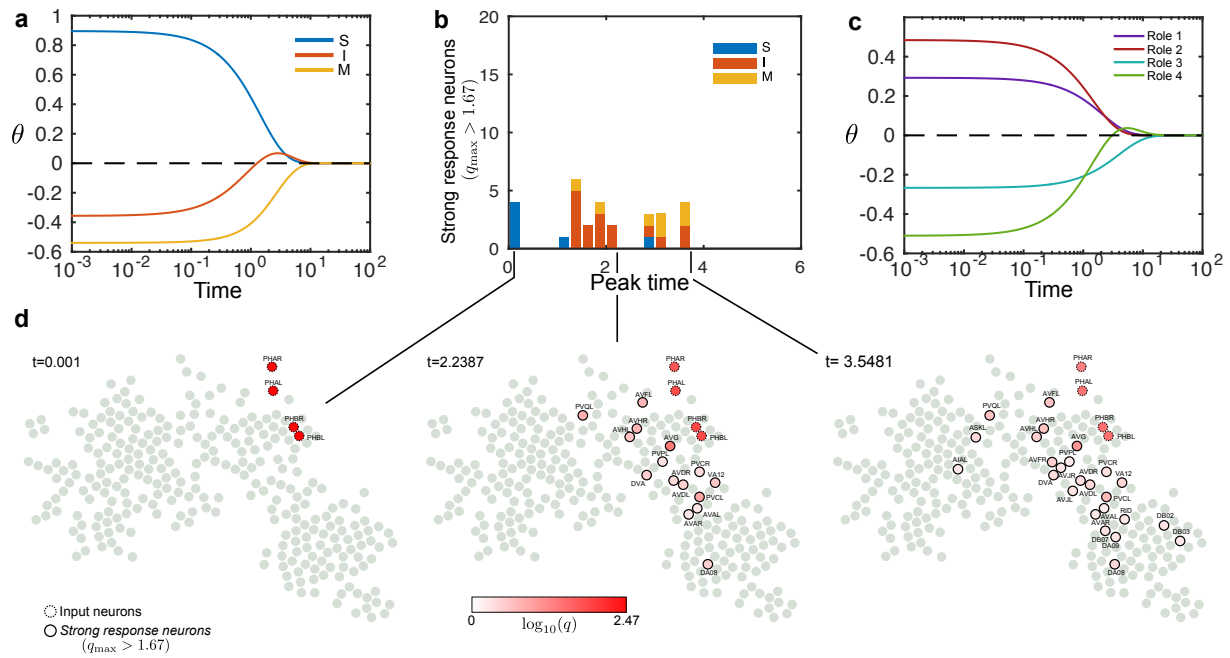


Figure S7. **Signal propagation: posterior chemosensory stimulus (i3).** See Caption Figure S6.

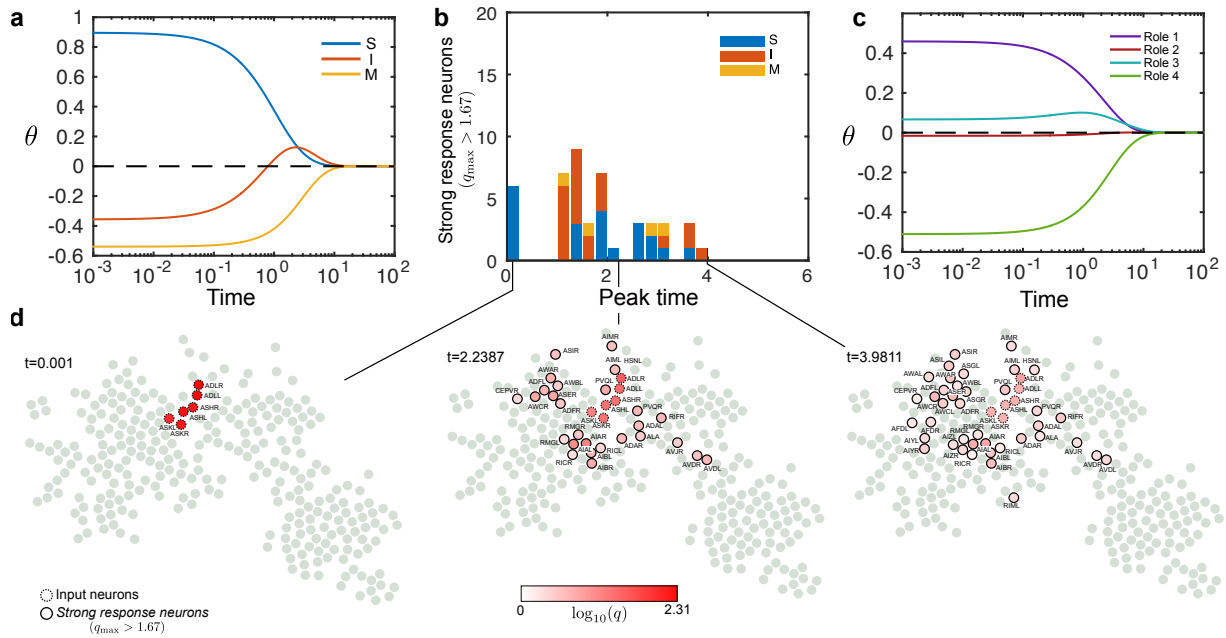


Figure S8. **Signal propagation: anterior chemosensory stimulus (i4).** See Caption Figure S6.

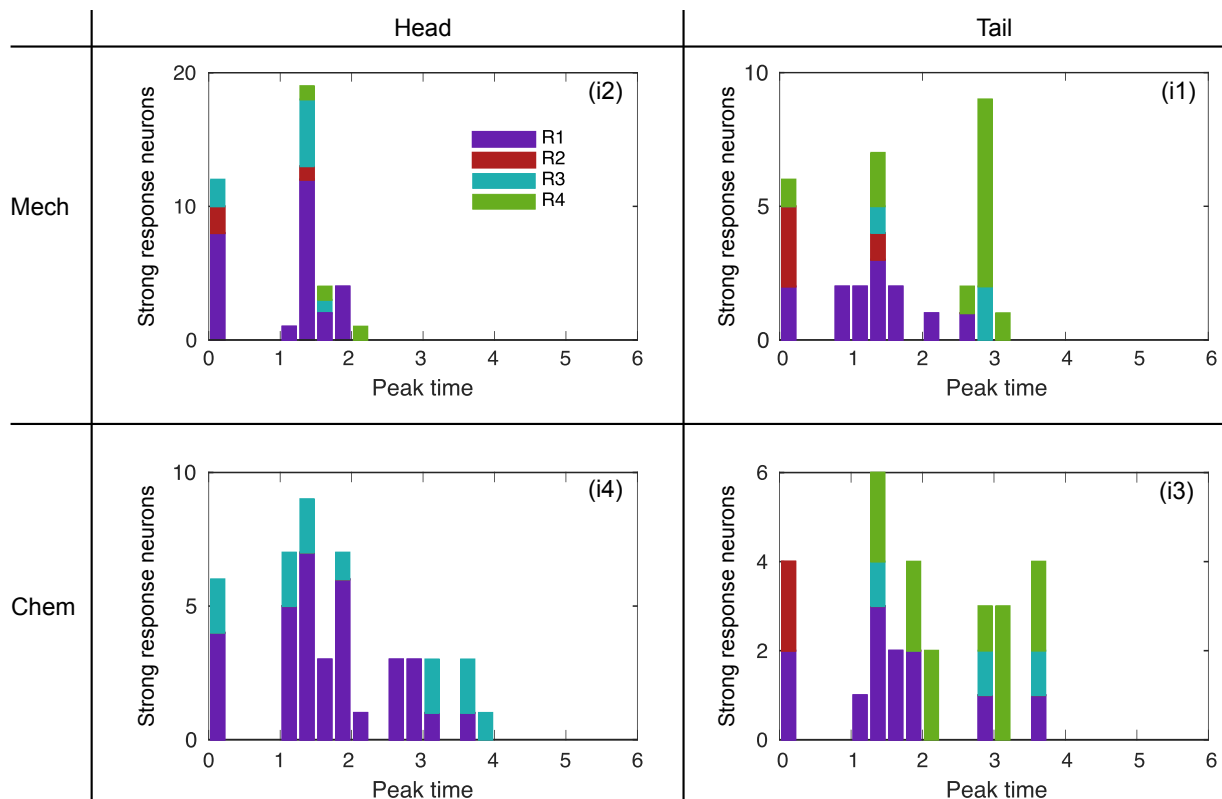


Figure S9. Peak times of strong response neurons summarised by RBS roles for each of the four input scenarios (i1)-(i4).

- [1] D. E. Donald, *C. elegans II* (Cold Spring Harbor Laboratory Press, 1997).
- [2] J. G. White, E. Southgate, J. N. Thomson, and S. Brenner, *Philosophical Transactions of the Royal Society of London. Series B, Biological Sciences* **314**, 1 (1986).
- [3] D. H. Hall and R. Russell, *The Journal of neuroscience* **11**, 1 (1991).
- [4] L. R. Varshney, B. L. Chen, E. Paniagua, D. H. Hall, and D. B. Chklovskii, *PLoS Computational Biology* **7** (2011).
- [5] M. Chalfie, J. E. Sulston, J. G. White, E. Southgate, J. N. Thomson, and S. Brenner, *The Journal of Neuroscience* **5**, 956 (1985).
- [6] T. Wakabayashi, I. Kitagawa, and R. Shingai, *Neuroscience Research* **50**, 103 (2004).
- [7] W. Li, L. Kang, B. J. Piggott, Z. Feng, and X. Z. S. Xu, *Nature communications* **2**, 315 (2011).
- [8] G. Nagel, M. Brauner, J. F. Liewald, N. Adeishvili, E. Bamberg, and A. G. A., *Current Biology* **15**, 2279 (2005).
- [9] S. Ibsen, A. T. C. Schutt, S. Esener, and S. H. Chalasani, *Nature Communications* **6** (2015).
- [10] G. J. Stephens, B. Johnson-Kerner, W. Bialek, and W. S. Ryu, *PLoS Comput. Biol.* **4**, e1000028 (2008).
- [11] E. Yemini, T. Jucikas, L. J. Grundy, A. E. Brown, and W. R. Schafer, *Nature methods* **10**, 877 (2013).
- [12] A. E. Brown, E. I. Yemini, L. J. Grundy, T. Jucikas, and W. R. Schafer, *Proceedings of the National Academy of Sciences* **110**, 791 (2013).
- [13] B. L. Chen, D. H. Hall, and D. B. Chklovskii, *Proceedings of the National Academy of Sciences of the United States of America* **103**, 4723 (2006).
- [14] D. J. Watts and S. H. Strogatz, *Nature* **393**, 440 (1998).
- [15] J. S. Kim and M. Kaiser, *Phil. Trans. R. Soc. B* **369** (2014).
- [16] A.-L. Barabási and R. Albert, *Science* **286**, 509 (1999).
- [17] E. K. Towilson, P. E. Vertes, S. E. Ahnert, W. R. Schafer, and E. T. Bullmore, *The Journal of Neuroscience* **33(15)**, 63806387 (2013).
- [18] A. Majewska and R. Yuste, *J Theor Biol* **212**, 155 (2001).
- [19] A. Arenas, A. Fernández, and S. Gómez, in *Bio-Inspired Computing and Communication* (Springer, 2008) pp. 9–18.
- [20] R. K. Pan, N. Chatterjee, and S. Sinha, *PLOS ONE* **5** (2010).
- [21] Y. Sohn, M.-K. Choi, Y.-Y. Ahn, J. Lee, and J. Jeong, *PLoS Comput. Biol.* **7** (2011).
- [22] D. M. Pavlovic, P. E. Vertes, E. T. Bullmore, W. R. Schafer, and T. E. Nichols, *PLoS ONE* **9(7)** (2014).

- [23] O. Sporns and R. F. Betzel, Annual review of psychology **67** (2015).
- [24] J.-C. Delvenne, S. N. Yaliraki, and M. Barahona, Proceedings of the National Academy of Sciences **107**, 12755 (2010), arXiv:0812.1811.
- [25] J.-C. Delvenne, M. T. Schaub, S. N. Yaliraki, and M. Barahona, in *Dynamics On and Of Complex Networks*, Vol. 2, edited by A. Mukherjee, M. Choudhury, F. Peruani, N. Ganguly, and B. Mitra (Springer New York, 2013) pp. 221–242.
- [26] R. Lambiotte, J. Delvenne, and M. Barahona, Network Science and Engineering, IEEE Transactions on **1**, 76 (2014), see also arXiv:0812.1770.
- [27] M. T. Schaub, J.-C. Delvenne, S. N. Yaliraki, and M. Barahona, PLoS ONE **7**, e32210 (2012).
- [28] M. Beguerisse-Díaz, G. Garduño Hernández, B. Vangelov, S. N. Yaliraki, and M. Barahona, J R Soc Interface **11** (2014), 10.1098/rsif.2014.0940.
- [29] K. Cooper and M. Barahona, arXiv:1012.2726 (2010), arXiv:1012.2726 [physics.soc-ph].
- [30] K. Cooper, *Complex Networks: Dynamics and Similarity*, Ph.D. thesis, University of London (2010).
- [31] M. Beguerisse-Díaz, B. Vangelov, and M. Barahona, in *2013 IEEE Global Conference on Signal and Information Processing (GlobalSIP)* (2013) pp. 937–940.
- [32] M. Hilliard, C. I. Bargmann, and P. Bazzicalupo, Current Biology **12**, 730 (2002).
- [33] Y. N. Billeh, M. T. Schaub, C. A. Anastassiou, M. Barahona, and C. Koch, Journal of neuroscience methods **236**, 92 (2014).
- [34] D. S. Bassett, D. L. Greenfield, A. Meyer-Lindenberg, D. R. Weinberger, S. W. Moore, and E. T. Bullmore, PLoS Comput Biol **6** (2010), 10.1371/journal.pcbi.1000748.
- [35] J. M. Gray, J. J. Hill, and C. I. Bargmann, PNAS **102**, 3184 (2005).
- [36] G. Haspel and M. J. O’Donovan, The Journal of Neuroscience **31(41)**, 14611 (2011).
- [37] M. T. Schaub, J. Lehmann, S. N. Yaliraki, and M. Barahona, Network Science **2**, 66 (2014).
- [38] L. A. Hardaker, E. Singer, R. Kerr, G. Zhou, and W. R. Schafer, Journal of Neurobiology **49**, 303 (2001).
- [39] D. Hall, Z. Altun, and L. Herndon, “Worm Atlas,” (2015).
- [40] Z. F. Altun, B. Chen, Z.-W. Wang, and D. H. Hall, Developmental Dynamics **238**, 1936 (2009).
- [41] F. Lorrain and H. C. White, The Journal of Mathematical Sociology **1**, 49 (1971).
- [42] M. G. Everett and S. P. Borgatti, The Journal of Mathematical Sociology **19**, 29 (1994).
- [43] T. A. Jarrell, Y. Wang, A. E. Bloniarz, C. A. Brittin, M. Xu, J. N. Thomson, D. G. Albertson, D. H. Hall, and S. W. Emmons, Science **337**, 437 (2012).
- [44] D. Edler and M. Rosvall, “The MapEquation software package, available online at <http://www.mapequation.org>,”.
- [45] R. Guimera and L. A. N. Amaral, Nature **433**, 895 (2005).
- [46] N. Chatterjee and S. Sinha, “Understanding the mind of a worm: hierarchical network structure underlying nervous system function in *C. elegans*,” in *Models of Brain and Mind - Physical, Computational and Psychological Approaches*, Progress in Brain Research, Vol. 168 (Elsevier, 2007) pp. 145–153.
- [47] A. Zaslaver, I. Liani, O. Shtangel, S. Ginzburg, L. Yee, and P. W. Sternberg, Proceedings of the National Academy of Sciences **112**, 1185 (2015).
- [48] C. Koch, *Biophysics of Computation* (Oxford University Press, 1999).
- [49] T. C. Ferree and S. R. Lockery, Journal of Computational Neuroscience **6**, 263 (1999).
- [50] M. B. Goodman, D. H. Hall, L. Avery, and S. R. Lockery, Neuron **20**, 763 (1998).
- [51] M. T. Schaub, Y. N. Billeh, C. A. Anastassiou, C. Koch, and M. Barahona, PLoS Computational Biology **11**, e1004196 (2015).
- [52] L. Page, S. Brin, R. Motwani, and T. Winograd, *The PageRank Citation Ranking: Bringing Order to the Web.*, Technical Report 1999-66 (Stanford InfoLab, 1999) previous number = SIDL-WP-1999-0120.
- [53] V. D. Blondel, J.-L. Guillaume, R. Lambiotte, and E. Lefebvre, Journal of Statistical Mechanics: Theory and Experiment **2008**, P10008 (2008).
- [54] B. Amor, S. N. Yaliraki, R. Woscholski, and M. Barahona, Mol. BioSyst. **10**, 2247 (2014).
- [55] M. Meilă, Journal of Multivariate Analysis **98**, 873 (2007).
- [56] C. E. Rasmussen and C. K. I. Williams, *Gaussian Processes for Machine Learning (Adaptive Computation and Machine Learning)* (The MIT Press, 2005).
- [57] R. Koenker, *Quantile regression*, 38 (Cambridge university press, 2005).
- [58] L. B. Smith and B. J. Reich, *BSquare: An R package for Bayesian simultaneous quantile regression*, Tech. Rep. (North Carolina State University, 2013).
- [59] M. T. Schaub, R. Lambiotte, and M. Barahona, Phys. Rev. E **86**, 026112 (2012).
- [60] S. P. Borgatti and M. G. Everett, Social Networks **15**, 361 (1993).